

FLUID FLOW AND HEAT TRANSFER
IN A SINGLE-PASS, RETURN-FLOW HEAT EXCHANGER

BY

SONG-LIN YANG

A DISSERTATION PRESENTED TO THE GRADUATE SCHOOL
OF THE UNIVERSITY OF FLORIDA IN
PARTIAL FULFILLMENT OF THE REQUIREMENTS
FOR THE DEGREE OF DOCTOR OF PHILOSOPHY

UNIVERSITY OF FLORIDA

1985

UNIVERSITY OF FLORIDA



3 1262 08552 3412

To My Family

ACKNOWLEDGMENTS

The author wishes to express his sincere appreciation to his graduate supervisory committee which included Dr. C. K. Hsieh, chairman; Dr. V. P. Roan; Dr. R. K. Irely; Dr. C. C. Hsu; and, Dr. H. A. Ingley, III. Special thanks go to his advisor, Dr. C. K. Hsieh, without whose suggestion of this research topic, guidance and helpful advice, this research would not have been possible.

The author also wishes to thank his wife, Li-Pin. Her patience and encouragement made his graduate study a beautiful memory.

Finally, the author wishes to acknowledge the Interactive Graphics Laboratory (IGL) and the Northeast Regional Data Center (NERDC) of the State University System of Florida for allowing him to utilize the computing facilities on campus.

TABLE OF CONTENTS

	Page
ACKNOWLEDGMENTS.....	iii
LIST OF TABLES.....	vi
LIST OF FIGURES.....	vii
NOMENCLATURE.....	ix
ABSTRACT.....	xiii
CHAPTER	
I INTRODUCTION.....	1
II FORMULATION OF PROBLEM.....	6
II.1 Governing Equations.....	6
II.2 Boundary Conditions.....	9
III GRID GENERATION AND CLUSTERING.....	12
III.1 Grid Generation in Domain A.....	14
III.2 Grid Clustering in Domain A.....	18
III.3 Grid Generation in Domain B and C.....	23
III.4 Evaluation of the Source Terms in Poisson's Equations.....	25
IV NUMERICAL SOLUTION.....	28
IV.1 Transformed Governing Equations and Boundary Conditions.....	28
IV.2 Discretization of Governing Equations and Boundary Conditions.....	31
IV.3 Numerical Solution Procedure.....	38
V EVALUATION OF PRESSURE DISTRIBUTION AND NUSSELT NUMBER.....	44
V.1 Pressure Distribution.....	44
V.2 Nusselt Number.....	49

VI	RESULTS AND DISCUSSION.....	53
VI.1	Velocity Field.....	53
VI.2	Wall Vorticity.....	59
VI.3	Pressure on Inner Wall.....	64
VI.4	Temperature Field.....	67
VI.5	Local Nusselt Number.....	73
VI.6	Mean Nusselt Number.....	75
VI.7	Truncation Error and Convergence.....	80
VII	CONCLUSIONS AND RECOMMENDATIONS.....	85
APPENDIX		
A	DERIVATION OF TRANSFORMATION RELATIONS, GOVERNING EQUATIONS, AND BOUNDARY CONDITIONS IN THE TRANSFORMED PLANE.....	88
B	DERIVATION AND USE OF EQUATION (3.6).....	105
C	DERIVATION OF FINITE DIFFERENCE EQUATIONS.....	108
D	DERIVATION OF PRESSURE GRADIENT EQUATIONS.....	119
	REFERENCES.....	122
	BIOGRAPHICAL SKETCH.....	125

LIST OF TABLES

Table		Page
1	Vortex Sizes for $Re=100, 500, \text{ and } 1000$	60
2	Inner-Wall Vorticity Data Near the Turning Point.....	63
3	Dimensionless Pressure Gradients at Exit.....	68
4	Comparison of the Computed Nusselt Number at the Exit with Lundberg's Data.....	78
5	Comparison of Mean Nusselt Number Between SPRF Heat Exchanger and Heating in a Circular Pipe.....	81
6	CPU Time Required for Computation of Stream Functions Given in Figure 22.....	84

LIST OF FIGURES

Figure		Page
1	A Schematic Showing the System Under Investigation.....	2
2	Specifications of the Single-Pass, Return-Flow Heat Exchanger.....	7
3	A Schematic Showing Mapping from the Physical Plane to the Computational Plane.....	13
4	Computed Grid Before and After Clustering in Domain A.....	19
5	Grid Detail Near the Inner Pipe Wall and the Turning Point.....	24
6	Complete Grid System.....	26
7	Block Diagram Showing the Numerical Procedure Used to Solve Stream Function and Vorticity.....	42
8	A Control Volume Used to Find the Mean Temperature by Energy Balance.....	51
9	Velocity Fields for $Re=100$, 500 , and 1000	54
10	Velocity Field Near Turning Point for $Re=100$	55
11	Velocity Field Near Turning Point for $Re=500$	56
12	Velocity Field Near Turning Point for $Re=1000$	57
13	Vorticity on the Inner Wall.....	61
14	Pressure Distribution on the Inner Wall.....	65
15	Isotherms for $Pr=0.7$ and $Re=100$, 500 , and 1000	69
16	Isotherms for $Pr=20$ and $Re=100$, 500 , and 1000	70

17	Isotherms for $Pr=100$ and $Re=100, 500,$ and 1000	71
18	Local Nusselt Number for $Pr=0.7$ and $Re=100,$ $500,$ and 1000	74
19	Local Nusselt Number for $Pr=20$ and $Re=100,$ $500,$ and 1000	76
20	Local Nusselt Number for $Pr=100$ and $Re=100,$ $500,$ and 1000	77
21	A Plot of Mean Nusselt Number.....	79
22	Comparison of the Computed Stream Functions Along Constant ξ -lines for Different Grid Systems.....	83
A.1	Schematic Showing Transformation from Physical to Transformed Plane.....	89
A.2	Unit Tangent and Normal Vectors on Lines of Constant ξ and η	98
A.3	Schematic Showing the Arc Length Along Contour Γ	100
B.1	Indexing z Axis for Eq. (B.4).....	106

NOMENCLATURE

a_1, a_2, a_3	coefficients defined in Eqs. (B.5) to (B.7)
C_h	dimensionless hydraulic diameter defined in Eq. (5.24), D_h/r_i
C_p	specific heat at constant pressure
C^+	constant defined in Eq. (5.7)
C1-C18	metric coefficients defined in Appendix C
C19-C28	coefficients defined in Chapter IV
D_h	hydraulic diameter
$\hat{e}_r, \hat{e}_\phi, \hat{e}_z$	unit vectors in the cylindrical coordinate system
F	scalar function
h	heat transfer coefficient
J	Jacobian of transformation
K	thermal conductivity
n	number of correlated point
\hat{n}	unit normal vector
Nu_z	local Nusselt number, hD_h/k
Nu_m	mean Nusselt number defined in Eq. (5.28)
P	source term defined in Eq. (3.26)
p	dimensionless pressure defined in Eq. (5.3), $p^*/(\rho u_m^2)$
p^*	pressure

p^+	normalized pressure defined in Eq. (5.10), $(\text{Rexp})/(8/C^+)$
P_{ex}	dimensionless pressure at exit, $p_{\text{ex}}^*/(\rho u_m^{*2})$
P_{fd}	dimensionless fully developed pressure, $P_{\text{fd}}^*/(\rho u_m^{*2})$
P_{ex}^*	pressure at exit section
P_{fd}^*	fully developed pressure
Pe	Peclet number, $PrxRe$
Pr	Prandtl number, $\mu C_p/K$
Q	source term defined in Eq. (3.27)
Re	Reynolds number, $\rho u_m^* r_i^*/\mu$
r	dimensionless radial coordinate, r/r_i^*
r_i	dimensionless inner pipe radius at inner pipe region, 1
r_{i0}	dimensionless inner pipe radius at annular region, r_{i0}^*/r_i^*
r_o	dimensionless outer pipe radius, r_o^*/r_i^*
r^*	radial coordinate in the cylindrical coordinate system
r_i^*	inner pipe radius at inner pipe region
r_{i0}^*	inner pipe radius at annular region
r_o^*	outer pipe radius
r^+	ratio of inner to outer radii, r_{i0}^*/r_o^*
S	arc length defined in Eq. (3.18)
\bar{S}	arc length defined in Eq. (3.17)
T	temperature
T_e	fluid inlet temperature
T_W	inner pipe wall temperature

t	surface coordinate
\hat{t}	unit tangent vector
u	dimensionless axial velocity, u^*/u_m^*
u^*	axial velocity
u_m^*	mean velocity
v	dimensionless radial velocity, v^*/u_m^*
v^*	radial velocity
W_1	relaxation factor for Eq. (4.31)
W_2	relaxation factor for Eq. (4.32)
W_r	relaxation factor for Eq. (3.16)
W_z	relaxation factor for Eq. (4.15)
W_ψ	relaxation factor for Eq. (4.19)
W_Ω	relaxation factor for Eq. (3.20)
W_Θ	relaxation factor for Eq. (3.21)
z	dimensionless axial coordinate, z^*/r_i^*
z^*	axial coordinate in the cylindrical coordinate system
ξ, η	transformed coordinates
ψ_i	normalized index defined in Eq. (3.7)
ψ	dimensionless stream function, $\psi^*/r_i^{*2}u_m^*$
ψ^*	stream function
Ω	dimensionless vorticity, $\Omega^*r_i^*/u_m^*$
Ω^*	vorticity
θ	dimensionless temperature, $(T_w - T)/(T_w - T_e)$
θ_m	dimensionless mean temperature defined in Eq. (5.25)
ρ	density

μ dynamic viscosity coefficient
 ϵ parameter defined in Eq. (3.20)
 ϕ angular coordinate in the cylindrical coordinate system
 α, β, γ metric coefficients defined in Eqs. (3.20) to (3.12)

SUBSCRIPTS

i, j denotes the grid point
 \max maximum
 n normal derivative
 r partial differentiation with respect to r
 w wall
 $wall$ wall value
 z partial differentiation with respect to z
 ξ partial differentiation with respect to ξ
 η partial differentiation with respect to η

SUPERSCRIPTS

k iteration count or inner iteration count
 n iteration count or outer iteration count
 ξ quantity that evaluated along constant ξ line
 η quantity that evaluated along constant η line

PREFIX

∇ gradient operator
 Δ difference operator
 d differential operator
 ∂ partial differential operator

Abstract of Dissertation Presented to the Graduate School
of the University of Florida in Partial Fulfillment of the
Requirements for the Degree of Doctor of Philosophy

FLUID FLOW AND HEAT TRANSFER
IN A SINGLE-PASS, RETURN-FLOW HEAT EXCHANGER

BY

SONG-LIN YANG

May, 1985

Chairman: C. K. Hsieh
Major Department: Mechanical Engineering

Numerical solutions for flow and heat transfer in a single-pass, return-flow heat exchanger are given for Reynolds numbers (Re) of 100, 500, and 1000, and Prandtl numbers (Pr) of 0.7, 20, and 100. The flow is modeled as laminar, axisymmetric, incompressible, and in steady state, and the Navier-Stokes equations are expressed in terms of stream function and vorticity.

Prior to the solution of the problem by means of a finite difference method, the original geometry of the system in the physical plane is transformed into a rectangular domain with square grids in a computational plane. Grid clustering techniques are also employed to reposition grid lines for good resolution in those regions where the flow and temperature fields change most

rapidly. The original partial differential equations are expressed in finite-difference forms, and in order to assure convergence in the numerical iteration, the matrix coefficients in the matrix equations are reconstructed to make those diagonal terms dominant in the coefficient matrix.

Numerical data indicate that the flow is accelerated in the end cap. There is a recirculation zone near the inner end of the inner pipe, where the main flow is separated from the wall. The mean Nusselt number for the exchanger is found to be proportional to the Reynolds number and the Prandtl number. The present exchanger has a mean Nusselt number that is about 1.57 to 1.87 times that for heat transfer in a singular pipe under similar operating conditions (Re and Pr number). The exchanger is thus shown to be effective in heat transfer.

CHAPTER I INTRODUCTION

The single-pass, return-flow (SPRF) heat exchanger shown in figure 1 consists of a circular pipe inserted inside an outer pipe. The outer pipe is sealed at one end so that fluid entering the inner pipe may be deflected into the annulus formed between the inner and the outer pipe of the exchanger. Either the inner or the outer pipe wall, or both, may be heated, and the heat input may be simulated by different conditions at these walls.

The heat exchanger described above is structurally similar to the bayonet tube studies by Hurd [1] in 1946; however, they serve different purposes. In the bayonet tube, the double-pipe construction is essentially used for transporting fluid. Hence, the entering and exiting fluids exchange heat with each other via the heat conducting inner wall, and whether heat is transferred in or out of the system depends on the temperature difference between the fluid in the annulus and the medium surrounding it at the shell side. This is not so, however, for the heat exchanger, in which the inner pipe wall may be heated. Then, the entering and exiting fluids both exchange heat with this wall, and the system becomes a compact,

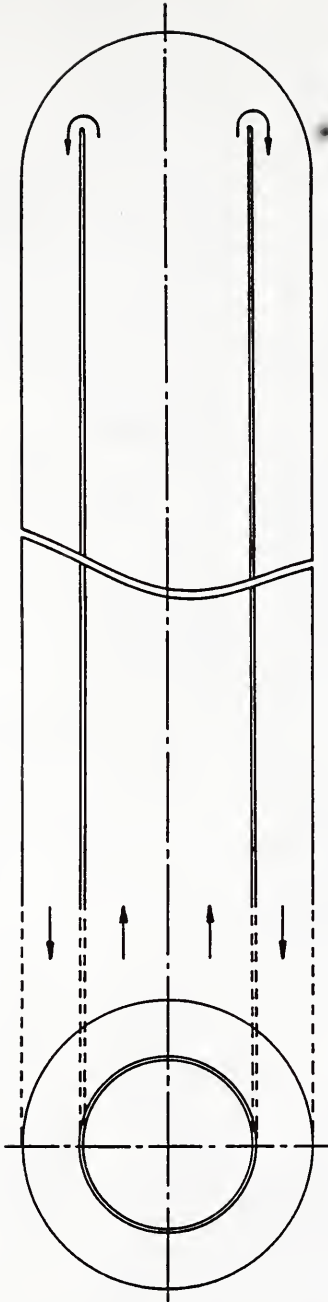


Figure 1 A Schematic Showing the System Under Investigation

stand-alone device. In fact, the exchanger possesses all the virtues of the bayonet tube, such as the freedom from stress-and-strain problems in the inner pipe and the ease of replacement of tubes in case of failure, while not suffering from the lack of versatility that usually handicaps the use of the bayonet tube.

A review of the literature reveals that there is a lack of basic research dealing with the heat exchanger. Hurd [1] studied the mean temperature difference in the bayonet tube for four different arrangements of fluid flow directions. Large temperature differences were found when flow direction in the annulus was counter to the flow direction of the heat exchanger medium at the shell side. A more recent study dealt with the use of the heat exchanger in solar collectors [2]. In this application, the outside pipe of the exchanger becomes the inner wall of a dewar, and the outside surface of this pipe is coated with a spectral selective coating to enhance its heat absorption. Owens-Illinois has used this concept in developing its SUNPAK collectors with success [3].

It is quite natural for one who is interested in fluid flow and heat transfer analysis to consider the SPRF exchanger as a combination of two separate components, circular pipe and annulus, because their fluid flow and heat transfer have been thoroughly studied in the literature, e.g. [4]. However, because of the presence of

the round cap at one end of the heat exchanger, the fluid flow in the upstream region may be affected by that in the downstream region. As a result, to divide the exchanger into two subsystems and to patch up their solutions at points of matching may be an oversimplification of this complicated problem. A realistic modelling of the system will require the treatment of the system as a single unit. This motivates the research of this dissertation.

In this work, the flow is assumed to be laminar, axisymmetric, incompressible, and in steady state. Stream function and vorticity are used in the solution of the problem (Chapter II). The original irregular geometry of the system in the physical plane is transformed to a rectangular domain with square grids in the computational plane. Grid lines are clustered to provide good resolution in regions where flow and temperature fields change most rapidly (Chapter III). The problem is solved numerically with an iterative scheme and, in order to assure a convergent solution, diagonal matrix elements in the governing matrix equation are maximized (Chapter IV). Pressure distribution and Nusselt number are evaluated at $Re=100$, 500 , and 1000 , and $Pr=0.7$, 20 , and 100 (Chapter V). Thus, laminar flow is stable and the use of the steady flow form of the governing equation is physically credible. Numerical results indicate that the SPRF exchanger is superior to heat transfer in a circular

pipe. The present exchanger has a mean Nusselt number that is about 1.57 to 1.87 times that for heat transfer in a singular pipe under similar operating conditions (Chapter VI).

CHAPTER II FORMULATION OF PROBLEM

The system under investigation is shown in figure 2, where the dimensional ratios of the pipes are also provided in the figure. Note that the thickness of the inner pipe is only one-hundredth of its radius, while the inner end of the pipe that is facing the spherical cap is rounded. The radius of the inner pipe was chosen such that the cross section of flow in the pipe is equal to the ring passage between the pipe and the cap, and this area is also equal to the cross section of the annulus region; see dashed line marks in the figure. The length of the pipes is approximately twelve times the radius of the inner pipe, a length short enough to show the entrance effect, yet long enough so that the boundary conditions imposed at the exit section of the annulus will have little effect on the flow conditions inside the annulus.

II.1 Governing Equations

For the problem under investigation, the flow is treated as steady, incompressible, and laminar. The fluid medium is assumed to have constant thermophysical properties. Both the flow and the temperature field are

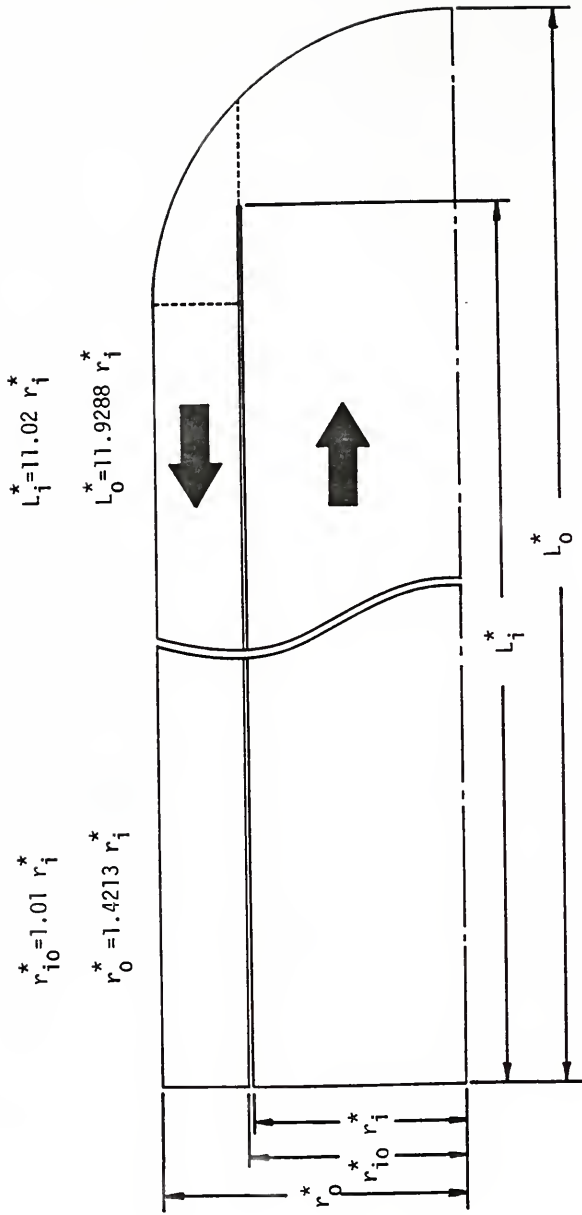


Figure 2 Specifications of the Single-Pass, Return-Flow Heat Exchanger

invariant in the ϕ direction; the flow is thus axisymmetrical, which also permits the use of the stream function in the analysis. It is further assumed that the Eckert number is small enough so that dissipation is negligible. Under these conditions, the momentum equations in r and z directions can be combined to derive the vorticity transport equation [5]

$$\frac{1}{r} \psi_r \Omega_z - \frac{1}{r} \psi_z \Omega_r + \frac{\Omega}{r^2} \psi_z = \frac{1}{\text{Re}} (\Omega_{zz} + \Omega_{rr} + \frac{1}{r} \Omega_r - \frac{\Omega}{r^2}) \quad (2.1)$$

where the vorticity Ω is related to the stream function ψ by the following relationship:

$$\psi_{zz} + \psi_{rr} - \frac{1}{r} \psi_r = -r\Omega \quad (2.2)$$

As usual, the stream function is related to the velocity u and v by

$$u = \frac{1}{r} \psi_r \quad (2.3)$$

$$v = -\frac{1}{r} \psi_z \quad (2.4)$$

The energy equation can be expressed in terms of stream function as

$$\frac{1}{r} \psi_r \theta_z - \frac{1}{r} \psi_z \theta_r = \frac{1}{\text{Pe}} (\theta_{zz} + \theta_{rr} + \frac{1}{r} \theta_r) \quad (2.5)$$

where Pe stands for the Peclet number, a product of the Prandtl number and the Reynolds number, $Pe=PrxRe$.

In the formulation given above, the spatial variables r and z have been made dimensionless by dividing the original r^* and z^* by r_i^* , the radius of the inner pipe. The velocities u and v have been normalized with reference to the mean velocity, u_m^* ; θ is a dimensionless temperature, defined as $\theta=(T_w-T)/(T_w-T_e)$, where T_w and T_e refer to the inner wall temperature and the fluid inlet temperature, respectively. There are five unknowns (u,v,θ,ψ,Ω) in these equations, and there are five equations to solve them.

II.2 Boundary Conditions

Because of the large number of conditions to be used in the analysis, it is convenient to summarize them according to the locations where they will be applied.

Inlet: The velocity and temperature are both uniform at the inlet. Here the v component of velocity is zero.

Exit: Because of the exit section being remote from the inlet section, u , v , ψ , and Ω are considered invariant in the z direction at exit. This assumption has been supported by a study in which it showed that the exact nature of the downstream condition had little effect on the solution of the problem [6]. It is further assumed that conduction

in the fluid is small at the exit section, a valid assumption for $Pe > 100$ as proposed by Singh [7].

Axis of symmetry: The first derivative of u and θ with r must be zero along the axis of symmetry. Here the velocity v is also zero.

Walls: Both u and v velocities vanish at the inner and outer pipe walls. Physically, to satisfy these conditions, the vorticity must be continuously generated at these walls. For heat transfer analysis, a constant temperature condition is imposed at the inner wall, while the outer wall is insulated.

The conditions mentioned above can be formulated as follows.

Inlet:

$$u = 1 \quad (2.6a)$$

$$v = 0 \quad (2.6b)$$

$$\theta = 1 \quad (2.6c)$$

$$\psi = \frac{r^2}{2} \quad (2.6d)$$

$$\Omega = 0 \quad (2.6e)$$

Exit:

$$u_z = v_z = \psi_z = \Omega_z = 0 \quad (2.7a)$$

$$\theta_{zz} = 0 \quad (2.7b)$$

Axis of symmetry:

$$u_r = v = \theta_r = \psi = \Omega = 0 \quad (2.8)$$

Inner pipe wall:

$$u = v = \theta = 0 \quad (2.9a)$$

$$\psi = \frac{1}{2} \quad (2.9b)$$

Outer pipe wall:

$$u = v = \theta_n = \psi = 0 \quad (2.10)$$

where the subscript n for θ denotes the normal derivative.

The missing vorticity conditions at the walls may be derived by using Eq. (2.2), in which a great simplification can be made by using the facts that (i) $u = v = 0$ at the walls, and (ii) the walls may be regarded as one of the streamlines. For the time being, this condition is expressed as

$$\Omega_w = - \left[\frac{1}{r} (\psi_{zz} + \psi_{rr} - \frac{1}{r} \psi_r) \right]_{\text{wall}} \quad (2.11)$$

It will be simplified later in Chapter IV.

CHAPTER III
GRID GENERATION AND CLUSTERING

Because of the irregularity of the geometry under investigation, the solution of the problem in the original physical plane is difficult. It is desirable to use grid generation techniques to transform the grid points in the physical plane to the computational plane so that computation can be conveniently carried out in the new plane.

Refer to the mapping diagrams shown in figure 3. The physical plane is in (z,r) coordinates, while the computational plane is in (ξ,η) coordinates. It is necessary to transform the domain abcdefghija in the physical plane to the domain $a^*b^*c^*d^*e^*f^*g^*h^*i^*j^*a^*$ in the computational plane, the mapping being one-to-one. Notice that the fluid enters the heat exchanger through the inner pipe, and the fluid actions are more intense near the wall and around the turning point (h) at the tip of the inner pipe; a fine grid is necessary to study the fluid flow and heat transfer in these regions. To facilitate grid generation to meet these requirements, the total system is subdivided into three domains: domain A in bcdghib, domain B in abija, and domain C in fgdef; and transformations will

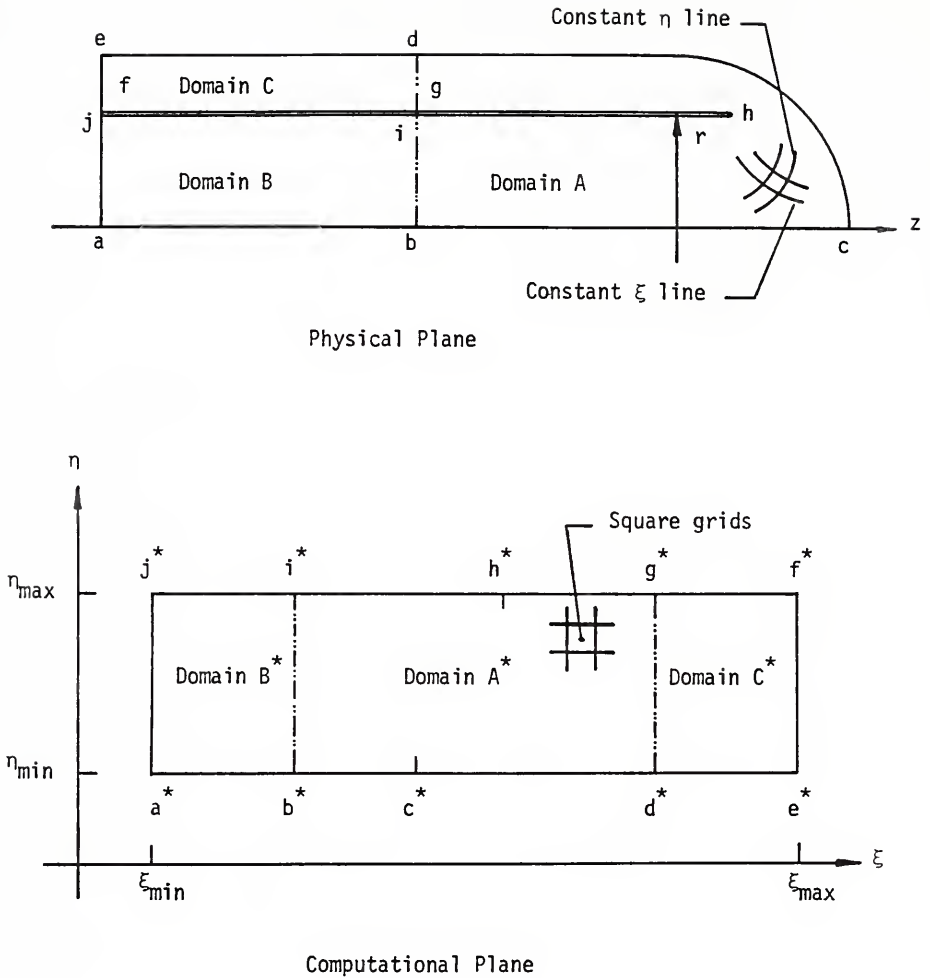


Figure 3 A Schematic Showing Mapping from the Physical Plane to the Computational Plane

be made separately in these regions to map the grid points from one plane to another. Also note that, after transformation, the streamlines in the physical plane will correspond roughly to the constant n lines in the computational plane.

The transformation will be accomplished in three steps. In the first step, the domain A will be mapped to domain A*. The next step is to fine-tune those grid lines in this domain so that a dense grid is formed close to the walls and near the turning point of the inner pipe. Finally, grids in domains B and C are filled in so that they match those grids already laid out in domain A. The details of these transformations will be spelled out in the three sections that follow.

III.1 Grid Generation in Domain A

Differential equation methods will be used to generate grids in domain A. Specifically, the elliptic partial differential equation technique developed by Thompson, Thames, and Mastin (TTM) will be used [8]. In order to simplify computation of the velocity and temperature fields to be made later, the grids in domain A* in the computational plane are taken to be squares, and Laplace equations

$$\xi_{zz} + \xi_{rr} = 0 \quad (3.1)$$

and

$$\eta_{zz} + \eta_{rr} = 0 \quad (3.2)$$

are used in the physical plane to generate those square grids in the computational plane; see figure 3. It can be shown (see Appendix A) that these equations are transformed to the following two in the computational plane

$$\alpha z_{\xi\xi} - 2\beta z_{\xi\eta} + \gamma z_{\eta\eta} = 0 \quad (3.3)$$

$$\alpha r_{\xi\xi} - 2\beta r_{\xi\eta} + \gamma r_{\eta\eta} = 0 \quad (3.4)$$

where

$$\alpha = z_{\eta}^2 + r_{\eta}^2, \quad \beta = z_{\xi}z_{\eta} + r_{\xi}r_{\eta}, \quad \gamma = z_{\xi}^2 + r_{\xi}^2 \quad (3.5)$$

It is imperative that the physical boundary of the inner pipe, that is, ihg , be mapped onto $i^*h^*g^*$, and bcd be mapped to $b^*c^*d^*$; both are constant η lines in the computational plane. Similar relations must be established for the bi and dg lines, which become constant ξ lines in the computational plane. These one-to-one mapping relations are usually referred to in the literature as boundary conditions for the transformation equations (3.3) and (3.4). In actuality, they provide the necessary conditions so that constant η lines conform to the physical boundary of the actual system.

To lay out z coordinates that enable a dense grid to be formed near the turning point h , a cubic polynomial

equation

$$z_i = z_0 + a_1 \psi_i + a_2 \psi_i^2 + a_3 \psi_i^3 \quad (3.6)$$

proposed by Nietubicz et al. is used [9]. The z_0 and z_i refer to the z positions at index i_0 and i_i , respectively; i_0 refers to the index at the turning point. ψ_i is a normalized index, given as

$$\psi_i = \frac{i_i - i_0}{i_f - i_0} \quad (3.7)$$

Equation (3.6) permits the z coordinates to be laid out with the size of the increment Δz increasing with the value of the index i_i . Once the positions of the first and last point on the z axis are fixed, and correspondingly, values for the indices i_0 and i_f are assigned, and with the provision of the sizes of the first and the last z increment as additional input, this equation can be used to generate an array of z positions having spacings as desired. The use of this equation is discussed fully in Appendix B.

Positions of interior nodal points (z,r) are found by solving Eqs. (3.3) and (3.4). Since these equations are nonlinear, a numerical technique must be used to solve them. In this method, all derivatives in these equations are represented by central differences, and the resulting

difference equations take the following form:

$$\alpha z_{i-1,j}^{-2(\alpha+\gamma)} z_{i,j}^{+\alpha} z_{i+1,j} = -\gamma (z_{i,j-1} + z_{i,j+1}) + \frac{\beta}{2} \bar{z}_{\xi\eta} \quad (3.8)$$

$$\alpha r_{i-1,j}^{-2(\alpha+\gamma)} r_{i,j}^{+\alpha} r_{i+1,j} = -\gamma (r_{i,j-1} + r_{i,j+1}) + \frac{\beta}{2} \bar{r}_{\xi\eta} \quad (3.9)$$

where

$$\alpha = \frac{1}{4} [(z_{i,j+1} - z_{i,j-1})^2 + (r_{i,j+1} - r_{i,j-1})^2] \quad (3.10)$$

$$\beta = \frac{1}{4} [(z_{i+1,j} - z_{i-1,j})(z_{i,j+1} - z_{i,j-1}) + (r_{i+1,j} - r_{i-1,j})(r_{i,j+1} - r_{i,j-1})] \quad (3.11)$$

$$\gamma = \frac{1}{4} [(z_{i+1,j} - z_{i-1,j})^2 + (r_{i+1,j} - r_{i-1,j})^2] \quad (3.12)$$

$$\bar{z}_{\xi\eta} = (z_{i+1,j+1} - z_{i+1,j-1} + z_{i-1,j-1} - z_{i-1,j+1}) \quad (3.13)$$

and

$$\bar{r}_{\xi\eta} = (r_{i+1,j+1} - r_{i+1,j-1} + r_{i-1,j-1} - r_{i-1,j+1}) \quad (3.14)$$

Iteration is used in conjunction with successive line over-relaxation to solve these equations. The relaxation procedure is formulated as follows for each η line (i.e., for a fixed j index):

$$z_{i,j}^{k+1} = z_{i,j}^k + w_z (z_{i,j} - z_{i,j}^k) \quad (3.15)$$

and

$$r_{i,j}^{k+1} = r_{i,j}^k + w_r (r_{i,j} - r_{i,j}^k) \quad (3.16)$$

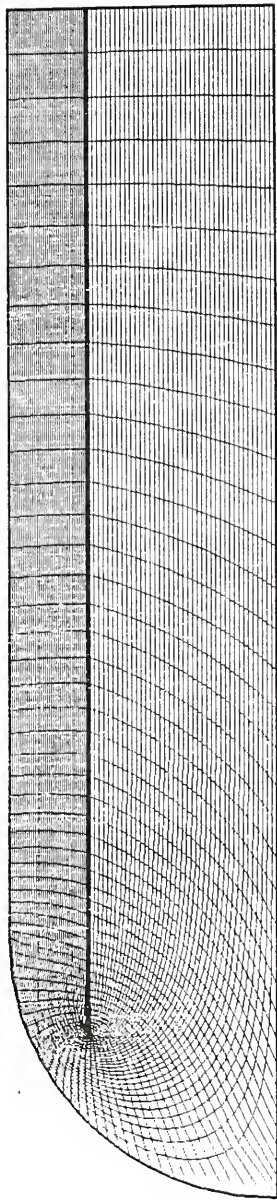
where $1 < i < i_{\max}$. In these equations, $z_{i,j}$ and $r_{i,j}$ are the solutions of Eqs. (3.8) and (3.9); w_z and w_r are relaxation parameters for z and r . The superscript k for z and r refers to the iteration count. In the iteration, the initial guess for the grid locations is made by using linear interpolation of those grid already located at the boundaries. It is found that a relaxation parameter of 1.7 yields fast convergence for both w_z and w_r , and the iteration is terminated if

$$\left| z_{i,j}^{k+1} - z_{i,j}^k \right| < 10^{-4} \quad \text{and} \quad \left| r_{i,j}^{k+1} - r_{i,j}^k \right| < 10^{-4}$$

The grid generated by the TTM solver is shown in figure 4 (a). The spacing along the z axis is satisfactory; however, the spacing in the r direction is not, which will be corrected later. It should be repeated that these grids are generated by using square grids in the computational plane. Also notice that, for the transformation made that is illustrated in this figure, 103 points are used along the z direction, 41 points in the r direction.

III.2 Grid Clustering in Domain A

The grids generated in the preceding section use Laplace equations for transformation. If Poisson's equations are used instead, the source terms in the



(a) Before Clustering



(b) After Clustering

Figure 4 Computed Grid Before and After Clustering in Domain A

Poisson's equations may be used to control grid positions, then a separate grid-line clustering effort may be spared. Sorenson and Steger found out that this method of clustering grid lines may lead to complexities or even unsatisfactory results in the computation [10]. For this reason, the grids are not transformed using Poisson's equations in this work; Laplace equations are used instead, and the generated grid lines are clustered later by means of clustering functions. In this effort, Sorenson and Steger's method will be used as described below.

The grid lines in the z direction have been laid out satisfactorily; no changes need be made of them. Lines in the r direction must be clustered so that a dense grid is where the change in the gradient of the flow variable is most rapid. In other words, lines of constant η in the physical plane must be repositioned for each line of constant ξ . This clustering of η lines can be accomplished in two steps as follows.

(1) The arc length along each constant ξ line in figure 4 (a) is computed with the following relation:

$$\bar{S}_{i,j+1} = \bar{S}_{i,j} + [(z_{i,j+1} - z_{i,j})^2 + (r_{i,j+1} - r_{i,j})^2]^{1/2} \quad (3.17)$$

Since the first point is indexed 1, $\bar{S}_{i,1} = 0$ for the sake of consistency. Note that j refers to the index for the j th line of constant η ; the arc length is computed for a

fixed i (or constant ξ). Equation (3.17) can be used to compute the arc length for each grid point in figure 4 (a), and this yields a table of $z_{i,j}$ and $r_{i,j}$ as functions $\bar{S}_{i,j}$.

This part of the work is essentially used for locating grid positions in the physical plane. Once they are found, the constant η lines in the physical plane may be discarded.

(2) The new grid lines in the physical plane will be laid out. An exponential stretching function is used so that the grid spacing between constant η lines increases monotonically with the value of j . The following relation meets this requirement.

$$S_{i,j+1} = S_{i,j} + \Delta S_0 (1+\epsilon)^{j-1} \quad (3.18)$$

Once again $S_{i,1} = 0$. In this equation, ΔS_0 is the desired minimum grid spacing near the wall of the outer pipe; ϵ is chosen such that $S_{i,j_{\max}} = \bar{S}_{i,j_{\max}}$. Equation (3.18) enables arc lengths, along a constant ξ line, to be found that give the desired grid locations for new η lines. The actual positions for these grids in the physical plane are found by interpolating the $z_{i,j}$ and $r_{i,j}$ tables constructed earlier.

There is one parameter ϵ that remains to be found in Eq. (3.18). As has been mentioned, this parameter controls the position of the outermost boundary, so

$$F(\varepsilon) = S_{i,j_{\max}} - \bar{S}_{i,j_{\max}} = 0 \quad (3.19)$$

The Newton-Raphson method may be used to find this ε . In this method, the n th iterated ε is expressed as

$$\varepsilon_i^n = \varepsilon_i^{n-1} - \frac{F(\varepsilon_i^{n-1})}{F'(\varepsilon_i^{n-1})} \quad (3.20)$$

where

$$F(\varepsilon_i^{n-1}) = \bar{S}_{i,j_{\max}} - \frac{\Delta S_0}{\varepsilon_i^{n-1}} [(1+\varepsilon_i^{n-1})^{j_{\max}-1} - 1] \quad (3.21)$$

and

$$F'(\varepsilon_i^{n-1}) = \frac{-\Delta S_0}{(\varepsilon_i^{n-1})^2} \{1 + (1+\varepsilon_i^{n-1})^{j_{\max}-2} \times [\varepsilon_i^{n-1} (j_{\max}-2) - 1]\} \quad (3.22)$$

Notice that this ε_i must be found for each ξ line in the reconstruction of new grids.

This clustering scheme described above monotonically increases the grid spacing away from the outer pipe wall. This creates a slight problem for those grids near the inner pipe wall because the rate of change of the gradient of the flow variable is also rapid there. It is necessary to cluster the grid lines near boundary ihg (figure 3) for good resolution. To accomplish this, an image method is employed as follows.

In the image method, the $S_{i,j_{\max}}$ in Eq. (3.18) is redefined to be $S_{i,j_{\max}}/2$, which length corresponds to that length to index $(j_{\max}+1)/2$, or to that line at its center. Then lines $[(j_{\max}+1)/2+1]$ to j_{\max} need not be regenerated but laid out by regarding them to be the mirror image of those lines from $[(j_{\max}+1)/2-1]$ to 1.

The clustered grid lines are shown in figure 4 (b), where ΔS_0 is 0.25% of the inner pipe radius. An enlarged grid near the turning point is shown in figure 5. The clustered grid lines appear to be uniformly distributed near the pipe wall and the turning point of the pipe. The grid generation task in domain A is thus completed.

III.3 Grid Generation in Domain B and C

The grid generation in domain B and C is rather straight-forward once the grids are laid out in domain A. Recall that the positions of the grid lines in the z direction in the physical plane are generated by using Eq. (3.6), in which values for z_0 , z_f , i_0 , i_f , Δz_1 , and Δz_f must be provided as input; the grid spacing increases with the index i . Then, in domain B, the z positions for the grid lines must be laid out from a to b because close to the inlet section a dense grid is desired. In domain C, however, the direction of z must be reversed because, at the exit section, the flow should approach fully developed; a dense grid there is unnecessary.

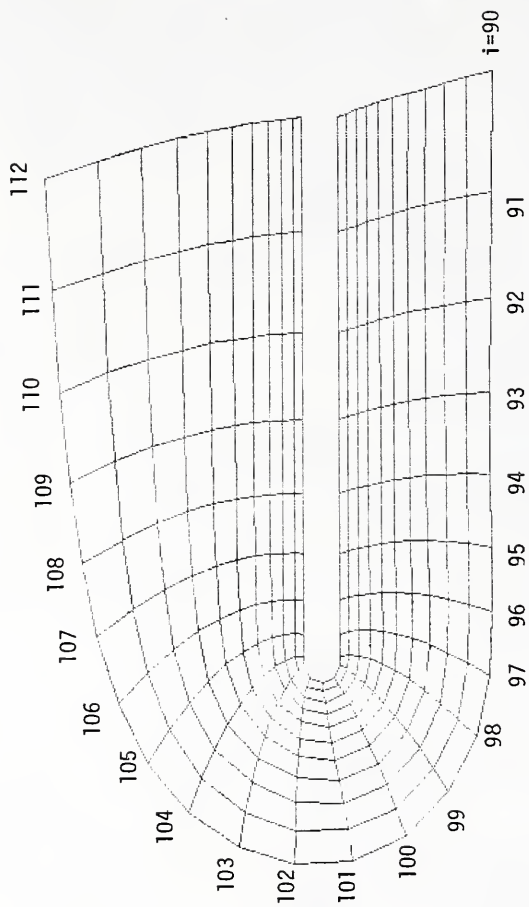


Figure 5 Grid Detail Near the Inner Pipe Wall and the Turning Point

As for the lines of constant η in domains B and C, a straight ray extension of those in domain A is adequate for this study. This method of grid generation results in an orthogonal non-uniform grid net in domains B and C. A plot of the finished grid is shown in figure 6. Because domains B and C are now linked to domain A, there are a total of 163 points in the z direction; the number of points across the flow passage in the r direction is still 41, which is unchanged.

III.4 Evaluation of the Source Terms in Poisson's Equations

The dense grids near the walls and the center line of the exchanger may be considered a result of heat sources and sinks. Hence, although Poisson's equations were not used to generate grids, the redistributed grid locations implicate that these source terms do present now; the original Laplace transformation relations are no longer valid, and the forcing functions in the Poisson's equations must now be determined.

It has been shown in Appendix A that these Poisson's equations in the computational plane are of the following form:

$$\alpha z_{\xi\xi} - 2\beta z_{\xi\eta} + \gamma z_{\eta\eta} = -J^2(Pz_{\xi} + Qz_{\eta}) \quad (3.23)$$

$$\alpha r_{\xi\xi} - 2\beta r_{\xi\eta} + \gamma r_{\eta\eta} = -J^2(Pr_{\xi} + Qr_{\eta}) \quad (3.24)$$

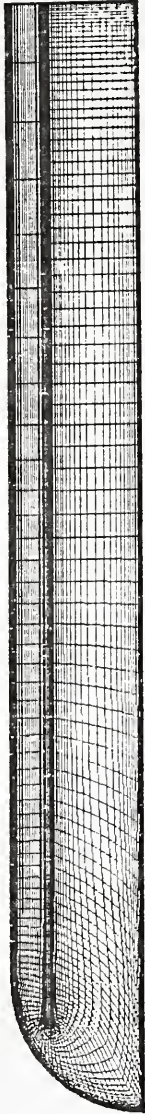


Figure 6 Complete Grid System

where J is the Jacobian of transformation

$$J = z_{\xi} r_{\eta} - z_{\eta} r_{\xi} \quad (3.25)$$

Equations (3.23) and (3.24) may be used to derive the source expressions as

$$P = (z_{\eta} Dr - r_{\eta} Dz) / J^3 \quad (3.26)$$

$$Q = (r_{\xi} Dr - z_{\xi} Dz) / J^3 \quad (3.27)$$

where

$$Dr = \alpha r_{\xi\xi} - 2\beta r_{\xi\eta} + \gamma r_{\eta\eta}$$

and

$$Dz = \alpha z_{\xi\xi} - 2\beta z_{\xi\eta} + \gamma z_{\eta\eta}$$

Equations (3.26) and (3.27) are to be solved numerically to find the forcing terms.

CHAPTER IV NUMERICAL SOLUTION

With the grids generated in the physical plane (z,r) , it is only necessary to solve the problem in the computational plane (ξ,η) so that a transformation back to the physical plane gives the final answers to the problem. The numerical solution of the problem is provided in this chapter. The governing equations and boundary conditions in the transformed plane will be given first in the section that follows.

IV.1 Transformed Governing Equations and Boundary Conditions

The governing equations in the computational plane are derived by using the partial differential identities given in Appendix A.

Vorticity transport equation:

$$\begin{aligned} & \alpha \Omega_{\xi\xi} - 2\beta \Omega_{\xi\eta} + \gamma \Omega_{\eta\eta} - \frac{J^2}{r^2} \Omega + (J^2 P - \frac{Jz}{r} \eta) \Omega_{\xi} + (J^2 Q + \frac{Jz}{r} \xi) \Omega_{\eta} \\ & = \frac{JRe}{r} [(\psi_{\eta} \Omega_{\xi} - \psi_{\xi} \Omega_{\eta}) + \frac{\Omega}{r^2} (r_{\eta} \psi_{\xi} - r_{\xi} \psi_{\eta})] \end{aligned} \quad (4.1)$$

Vorticity definition equation:

$$\begin{aligned} \alpha \psi_{\xi\xi} - 2\beta \psi_{\xi\eta} + \gamma \psi_{\eta\eta} + (J^2 P + \frac{Jz_{\eta}}{r}) \psi_{\xi} + (J^2 Q - \frac{Jz_{\xi}}{r}) \psi_{\eta} \\ = - J^2 r \Omega \end{aligned} \quad (4.2)$$

Velocity equations:

$$u = \frac{1}{Jr} (z_{\xi} \psi_{\eta} - z_{\eta} \psi_{\xi}) \quad (4.3)$$

$$v = \frac{1}{Jr} (r_{\xi} \psi_{\eta} - r_{\eta} \psi_{\xi}) \quad (4.4)$$

Energy equation:

$$\begin{aligned} \alpha \theta_{\xi\xi} - 2\beta \theta_{\xi\eta} + \gamma \theta_{\eta\eta} + (J^2 P - \frac{Jz_{\eta}}{r}) \theta_{\xi} + (J^2 Q + \frac{Jz_{\xi}}{r}) \theta_{\eta} \\ = \frac{JPe}{r} (\psi_{\eta} \theta_{\xi} - \psi_{\xi} \theta_{\eta}) \end{aligned} \quad (4.5)$$

Boundary conditions can be derived accordingly (Appendix A). Notice that, in the application of boundary conditions, all conditions of the first kind will be used as is; no transformations of them need be made. Other conditions must be changed to the computational plane, and they are listed together with those first-kind conditions below.

Inlet:

$$u = 1 \quad (4.6a)$$

$$v = 0 \quad (4.6b)$$

$$\theta = 1 \quad (4.6c)$$

$$\psi = \frac{r^2}{2} \quad (4.6d)$$

$$\Omega = 0 \quad (4.6e)$$

Exit:

$$u_\xi = v_\xi = \psi_\xi = \Omega_\xi = 0 \quad (4.7a)$$

$$\theta_{\xi\xi} = \frac{z_{\xi\xi}}{z_\xi} \theta_\xi \quad (4.7b)$$

Axis of symmetry:

$$z_\xi u_\eta - z_\eta u_\xi = 0 \quad (4.8a)$$

$$v = 0 \quad (4.8b)$$

$$z_\xi \theta_\eta - z_\eta \theta_\xi = 0 \quad (4.8c)$$

$$\psi = \Omega = 0 \quad (4.8d)$$

Inner pipe wall:

$$u = v = \theta = 0 \quad (4.9a)$$

$$\psi = \frac{1}{2} \quad (4.9b)$$

Outer pipe wall:

$$u = v = 0 \quad (4.10a)$$

$$\gamma \theta_\eta - \beta \theta_\xi = 0 \quad (4.10b)$$

$$\psi = 0 \quad (4.10c)$$

Notice that at both inner and outer walls, the vorticity boundary conditions can be expressed as

$$\Omega_w = - \frac{\gamma}{J^2 r} \psi_{\eta\eta} \quad (4.11)$$

Derivations of these expressions are given in the appendix.

IV.2 Discretization of Governing Equations and Boundary Conditions

Those governing equations given above will be solved numerically. In the solution, the grids are indexed as (i,j) , with i pointed in ξ direction and j in η direction. The governing equations are discretized as follows.

Vorticity transport equation:

$$\begin{aligned} [C7 + \text{Re}(C17\bar{\psi}_\xi - C18\bar{\psi}_\eta)] \Omega_{i,j} = \\ (C8 - \text{Re}C16\bar{\psi}_\eta) \Omega_{i+1,j} + (C9 + \text{Re}C16\bar{\psi}_\eta) \Omega_{i-1,j} \\ + (C10 + \text{Re}C16\bar{\psi}_\xi) \Omega_{i,j+1} + (C11 - \text{Re}C16\bar{\psi}_\xi) \Omega_{i,j-1} + C0\bar{\Omega}_{\xi\eta} \end{aligned} \quad (4.12)$$

Vorticity definition equation:

$$\begin{aligned} C1\psi_{i,j} = C2\psi_{i+1,j} + C3\psi_{i-1,j} + C4\psi_{i,j+1} + C5\psi_{i,j-1} \\ + C6\Omega_{i,j} + C0\bar{\psi}_{\xi\eta} \end{aligned} \quad (4.13)$$

Velocity equations:

$$u_{i,j} = C12\bar{\psi}_\eta - C13\bar{\psi}_\xi \quad (4.14)$$

$$v_{i,j} = C14\bar{\psi}_\eta - C15\bar{\psi}_\xi \quad (4.15)$$

Energy equation:

$$\begin{aligned}
 C10\theta_{i,j} = & (C8 - PeC16\bar{\psi}_\eta)\theta_{i+1,j} + (C9 + PeC16\bar{\psi}_\eta)\theta_{i-1,j} \\
 & + (C10 + PeC16\bar{\psi}_\xi)\theta_{i,j+1} + (C11 - PeC16\bar{\psi}_\xi)\theta_{i,j-1} \\
 & + CO\bar{\theta}_{\xi\eta}
 \end{aligned} \tag{4.16}$$

In these equations, CO through C18 represent metric coefficients listed in Appendix C. Those ψ , ω , and θ topped with bars are compact expressions for their increments in i and j directions; for example,

$$\bar{\psi}_\xi = \psi_{i+1,j} - \psi_{i-1,j}$$

$$\bar{\psi}_\eta = \psi_{i,j+1} - \psi_{i,j-1}$$

and

$$\bar{\psi}_{\xi\eta} = \psi_{i+1,j+1} - \psi_{i+1,j-1} + \psi_{i-1,j-1} - \psi_{i-1,j+1}$$

It is strictly a matter of computer programming expediency that these substitutions are made.

The discretized equations given above can be solved by an iterative method, in which the problems encountered include the nonlinearity of the vorticity transport equation and the high convection rate in the energy equation. Although use of an under-relaxation scheme in the iterative method may ease these problems, a small relaxation factor means an excessive computer time. For

these reasons, the matrix coefficients in the matrix equations are reconstructed to make those diagonal elements dominant in the coefficient matrix so that an iteration will yield a convergent solution.

The method used for maximizing the matrix elements is somewhat similar to the scheme developed by Takemitsu [11] and is rooted in the up-wind scheme that is commonly used in finite-differencing flow terms in the solution of fluid dynamics problems [12]. The vorticity transport equation is expressed as

$$C19\Omega_{i,j} = C20\Omega_{i+1,j} + C21\Omega_{i-1,j} + C22\Omega_{i,j+1} + C23\Omega_{i,j-1} + C0\bar{\Omega}_{\xi n} \quad (4.17)$$

This equation is a compact version of the vorticity equation derived in Appendix C, Eq. (C.35).

The energy equation is derived as

$$C24\theta_{i,j} = C25\theta_{i+1,j} + C26\theta_{i-1,j} + C27\theta_{i,j+1} + C28\theta_{i,j-1} + C0\bar{\theta}_{\xi n} \quad (4.18)$$

In both equations, C19 through C28 represent

$$C19 = C7 + \text{Re} [C17\bar{\psi}_{\xi} - C18\bar{\psi}_n + 2(|C16\bar{\psi}_{\xi}| + |C16\bar{\psi}_n|)]$$

$$C20 = C8 - \text{Re} (C16\bar{\psi}_n - |C16\bar{\psi}_n|)$$

$$C21 = C9 + \text{Re}(C16\bar{\psi}_n + |C16\bar{\psi}_n|)$$

$$C22 = C10 + \text{Re}(C16\bar{\psi}_\xi + |C16\bar{\psi}_\xi|)$$

$$C23 = C11 - \text{Re}(C16\bar{\psi}_\xi - |C16\bar{\psi}_\xi|)$$

$$C24 = C1 + 2\text{Pe}(|C16\bar{\psi}_\xi| + |C16\bar{\psi}_n|)$$

$$C25 = C8 - \text{Pe}(C16\bar{\psi}_n - |C16\bar{\psi}_n|)$$

$$C26 = C9 + \text{Pe}(C16\bar{\psi}_n + |C16\bar{\psi}_n|)$$

$$C27 = C10 + \text{Pe}(C16\bar{\psi}_\xi + |C16\bar{\psi}_\xi|)$$

and

$$C28 = C11 - \text{Pe}(C16\bar{\psi}_\xi - |C16\bar{\psi}_\xi|)$$

Successive-over-relaxation (SOR) methods will be used to solve these equations. In this method, the SOR versions of (4.13), (4.17), and (4.18) are, respectively,

$$\begin{aligned} \psi_{i,j}^{k+1} = & (1-w_\psi)\psi_{i,j}^k + \frac{w_\psi}{C1} (C2\psi_{i+1,j}^k + C3\psi_{i-1,j}^{k+1} \\ & + C4\psi_{i,j+1}^k + C5\psi_{i,j-1}^{k+1} + C6\Omega_{i,j}^{n+1} + C0\bar{\psi}_{\xi n}^*) \end{aligned} \quad (4.19)$$

$$\begin{aligned} \Omega_{i,j}^{k+1} = & (1-w_\Omega)\Omega_{i,j}^k + \frac{w_\Omega}{C19} (C20\Omega_{i+1,j}^k + C21\Omega_{i-1,j}^{k+1} \\ & + C22\Omega_{i,j+1}^k + C23\Omega_{i,j-1}^{k+1} + C0\bar{\psi}_{\xi n}^*) \end{aligned} \quad (4.20)$$

and

$$\begin{aligned} \theta_{i,j}^{k+1} = & (1-w_\theta)\theta_{i,j}^k + \frac{w_\theta}{C24} (C25\theta_{i+1,j}^k + C26\theta_{i-1,j}^{k+1} \\ & + C27\theta_{i,j+1}^k + C28\theta_{i,j-1}^{k+1} + C0\bar{\theta}_{\xi n}^*) \end{aligned} \quad (4.21)$$

where w_ψ , w_Ω , and w_θ denote the relaxation factors for ψ , Ω , and θ , respectively. Superscript k represents the inner iteration count in the numerical solution; the superscript n for $\Omega_{i,j}$ in (4.19) stands for the outer iteration count discussed later. The cross-derivative terms $\bar{\psi}_{\xi n}^*$, $\bar{\Omega}_{\xi n}^*$, and $\bar{\theta}_{\xi n}^*$ are evaluated using

$$\bar{\psi}_{\xi n}^* = \psi_{i+1,j+1}^k - \psi_{i+1,j-1}^{k+1} + \psi_{i-1,j-1}^{k+1} - \psi_{i-1,j+1}^k$$

$$\bar{\Omega}_{\xi n}^* = \Omega_{i+1,j+1}^k - \Omega_{i+1,j-1}^{k+1} + \Omega_{i-1,j-1}^{k+1} - \Omega_{i-1,j+1}^k$$

and

$$\bar{\theta}_{\xi n}^* = \theta_{i+1,j+1}^k - \theta_{i+1,j-1}^{k+1} + \theta_{i-1,j-1}^{k+1} - \theta_{i-1,j+1}^k$$

Iterations sweeps run from $i=1$ to i_{\max} and $j=1$ to j_{\max} .

Discretization of the governing equations is now complete; attention will now be directed to the boundary conditions which must be processed accordingly. In the discretization of boundary conditions, it must be noted that, in the numerical solution to be given later, ψ and Ω must be solved prior to the solution of the velocity and temperature fields. It is thus appropriate to discretize the ψ and Ω conditions first. In doing so, conditions of

the first kind will again be used as is. Therefore, only conditions of the second kind will be addressed. These second-kind conditions will be discretized in the order of their appearance in conditions (4.6) to (4.11) below.

The exit conditions Eq. (4.7a) are discretized by using a second-order central-difference scheme. At the exit section, for example, $\psi_{\xi} = 0$ is discretized to be

$$\psi_{i_{\max}+1,j} = \psi_{i_{\max}-1,j} \quad (4.22)$$

This identity will be used to substitute the values of ψ at index $(i_{\max}+1,j)$ when the difference equation (4.13) is evaluated at the exit section. This method also applies to Ω , u , and v .

The wall vorticity conditions (4.11) are approximated by the relation

$$\Omega_{i,w} = \frac{\gamma}{J^2 r} [2(\psi_{i,w+1} - \psi_{i,w})] \quad (4.23)$$

Here the bracketed terms are used to approximate $-\psi_{\eta\eta}$, and subscript $(w+1)$ for ψ refers to the grid location being one point away from the wall. This equation has only first-order accuracy but is adequate for use in the present work because of its conservation property as reported by Parmentier and Torrance [13].

Conditions for θ and u are treated next, and it is noted that, at the exit, the grids are orthogonal and $\psi_\xi = 0$. Equation (4.5) reduces to

$$\alpha \theta_{\xi\xi} + \gamma \theta_{\eta\eta} + J^2 P \theta_\xi + (J^2 Q + \frac{Jz_\xi}{r}) \theta_\eta = \frac{JPe}{r} \psi_\eta \theta_\xi \quad (4.24)$$

With the use of Eq. (4.7b) and after simplification, Eq. (4.24) becomes

$$\gamma \theta_{\eta\eta} + (J^2 Q + \frac{Jz_\xi}{r}) \theta_\eta = \frac{JPe}{r} \psi_\eta \theta_\xi \quad (4.25)$$

Central difference formula is then used to approximate all n -derivative quantities, and θ_ξ is discretized by the second-order backward difference, giving

$$\theta_\xi = \frac{1}{2} (\theta_{i_{\max}-2,j} - 4\theta_{i_{\max}-1,j} + 3\theta_{i_{\max},j}) \quad (4.26)$$

Along the axis of symmetry, Eq. (4.8a) is approximated by

$$u_{i,1} = \frac{1}{(z_n/z_\xi)+1} [u_{i,2} + (z_n/z_\xi)u_{i-1,1}] \quad (4.27)$$

in which the original u_ξ and u_η have been approximated by

$$(u_\xi)_{i,1} = u_{i,1} - u_{i-1,1}$$

$$(u_n)_{i,1} = u_{i,2} - u_{i,1}$$

again a first-order approximation.

Temperature condition along the same axis is treated in a similar manner,

$$\theta_{i,1} = \frac{1}{(z_n/z_\xi)+1} [\theta_{i,2} + (z_n/z_\xi)\theta_{i-1,1}] \quad (4.28)$$

At the outer pipe wall,

$$\theta_{i,1} = \frac{1}{(\beta/\gamma)+1} [\theta_{i,2} + (\beta/\gamma)\theta_{i-1,1}] \quad (4.29)$$

IV.3 Numerical Solution Procedure

A close examination of Eqs. (4.13) to (4.15), (4.17), (4.18), and (4.23) reveals that

- (1) the ψ equation, (4.13), contains all ψ but one Ω term;
- (2) the Ω equation, (4.17), contains both ψ and Ω terms;
- (3) ψ and Ω are also related in the wall vorticity condition, Eq. (4.23);
- (4) u and v are functions of ψ only; see Eqs. (4.14) and (4.15);
- (5) the θ equation (4.18), contains both ψ and θ terms.

These characteristics implicate that

- (1) ψ and Ω should be solved for simultaneously first;
- (2) θ , u , and v are solved next, with the use of ψ as input.

Based on these observations, an algorithm is developed as follows:

- (1) make an initial guess of ψ and Ω values at all grid points and assign these values as $\psi_{i,j}^1$ and $\Omega_{i,j}^1$,
- (2) update Ω values at the wall using (4.23)

$$\Omega_{i,w} = \frac{2\gamma}{j^2 r} (\psi_{i,w+1}^n - \psi_{i,w}^n) \quad (4.30)$$

- (3) calculate new values of Ω from (4.20) using SOR until convergence is attained; assign these values as $\Omega_{i,j}$ and then damp them by using

$$\Omega_{i,j}^{n+1} = \Omega_{i,j}^n + w_1 (\Omega_{i,j} - \Omega_{i,j}^n) \quad (4.31)$$

- (4) calculate new values of ψ from (4.19), again using SOR, until convergence is attained; assign these values as $\psi_{i,j}$ and then relax them by using

$$\psi_{i,j}^{n+1} = \psi_{i,j}^n + w_2 (\psi_{i,j} - \psi_{i,j}^n) \quad (4.32)$$

- (5) repeat steps (2) to (4) until both Ω and ψ converge.

Notice that in steps (3) and (4) above, iteration is used to find convergent Ω and ψ values for each set of assumed (or revised) and updated Ω and ψ values; these two steps are then called the inner iteration in the numerical solution. Steps (2) and (5), which repeat the total effort by renewing Ω and ψ values, are thus called the outer iteration.

Based on the experience of numerical work accumulated in the solution of this problem, $w_\psi = 1.5$ and $w_\Omega = 0.17$ yield convergent solutions; w_1 and w_2 are both taken to be 0.3, following the work by Rigal [14]. These relaxation parameters are used consistently for all Reynolds numbers tested in this work. In the numerical solution, results for ψ and Ω calculated for low Reynolds-number cases are used as the initial guess for high Reynolds-number cases. Thus, for example, the output of ψ and Ω for $Re=100$ is used as input for $Re=500$ case in step (1). For $Re=100$, the initial guess of the vorticity values is taken to be zero throughout. As for the stream function, a uniform flow is assumed.

The convergence criteria adopted are delineated as follows.

- (i) The convergence for outer iteration is set at

$$\left| \Omega_{i,w}^{n+1} - \Omega_{i,w}^n \right| < 10^{-4}$$

which also enables the following conditions to be met [15]:

$$\left| \psi_{i,j}^{n+1} - \psi_{i,j}^n \right| < 10^{-4} \quad \text{and} \quad \left| \Omega_{i,j}^{n+1} - \Omega_{i,j}^n \right| < 10^{-4}$$

(ii) The convergence for inner iteration of Eqs. (4.19) and (4.20) is set at

$$\left| \psi_{i,j}^{k+1} - \psi_{i,j}^k \right| < 10^{-3} \quad \text{and} \quad \left| \Omega_{i,j}^{k+1} - \Omega_{i,j}^k \right| < 10^{-3}$$

The inner iteration steps are limited to 50 in order to prevent it from converging to an erroneous solution [5]. It was found that once the outer iteration has converged as desired, the inner convergence criterion can be met with just one iteration. A flow chart for the numerical procedure is given in figure 7.

Once the stream function is found, the velocity field is calculated from Eqs. (4.14) and (4.15) and the energy equation can be solved in a straight-forward manner. In the solution of the energy equation, the second-kind boundary conditions are treated explicitly. Miyakoda's method [16] is used in this effort, in which the derivative boundary conditions are incorporated into nodal equations for interior nodes that are located one point away from the insulated boundary (that is, the center line or the outer wall). Hence, one point away from the center line,

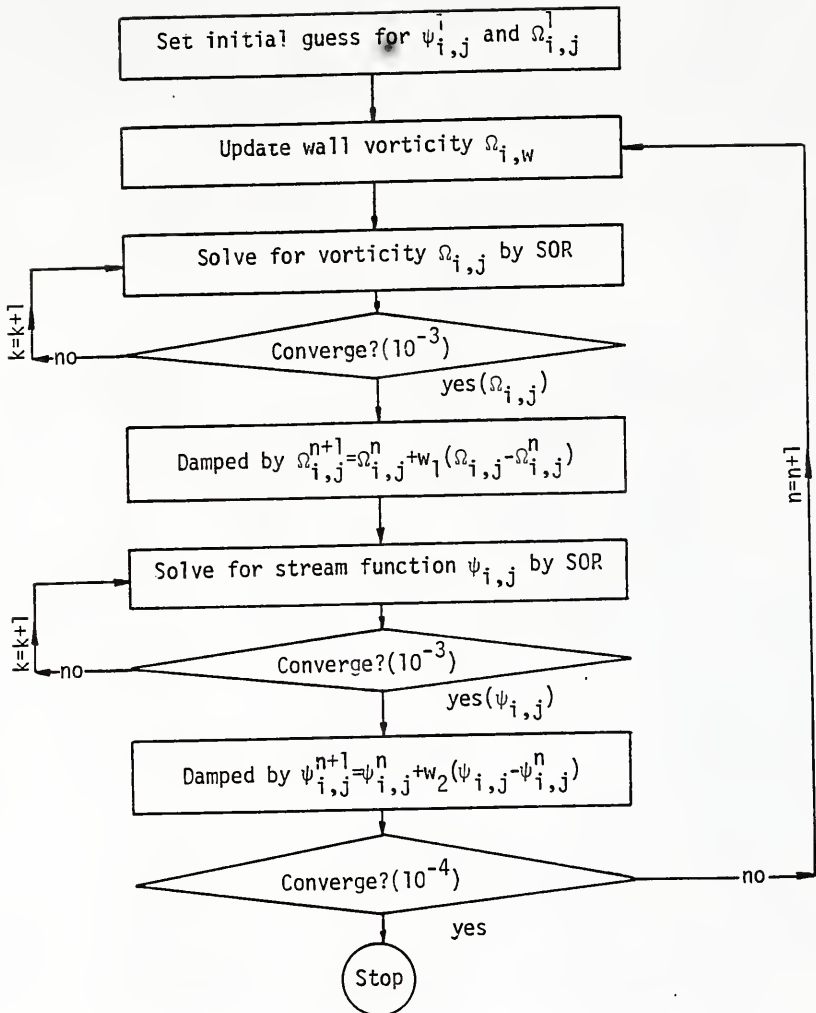


Figure 7 Block Diagram Showing the Numerical Procedure Used to Solve Stream Function and Vorticity

$$\begin{aligned}
 [C23 - \frac{1}{(z_n/z_\xi)+1}] \theta_{i,2} = C24 \theta_{i+1,2} + C25 \theta_{i-1,2} + C26 \theta_{i,3} \\
 + C27 \frac{z_n/z_\xi}{(z_n/z_\xi)+1} \theta_{i-1,1} + C0 \bar{\theta}_{\xi n} \quad (4.33)
 \end{aligned}$$

and one point away from the outer wall

$$\begin{aligned}
 [C23 - \frac{1}{(\beta/\gamma)+1}] \theta_{i,2} = C24 \theta_{i+1,2} + C25 \theta_{i-1,2} + C26 \theta_{i,3} \\
 + C27 \frac{\beta/\gamma}{(\beta/\gamma)+1} \theta_{i-1,1} + C0 \bar{\theta}_{\xi n} \quad (4.34)
 \end{aligned}$$

It is also noted that, before applying these equations to find $\theta_{i,2}$, $\theta_{i-1,1}$ must be updated by using (4.28) and (4.29). The relaxation parameter w_0 is taken to be 0.7 for all cases studied. A fast convergence results if the iteration proceeds from $i=1$ to i_{\max} , that is following the flow direction, and $j=j_{\max}$ to 1, that is, from the inner wall to the outer wall.

CHAPTER V
EVALUATION OF PRESSURE DISTRIBUTION AND NUSSELT NUMBER

Of the numerous quantities of interest in fluid flow and heat transfer, the pressure drop and the heat transfer coefficient are most important. The flow and temperature fields evaluated in the numerical solution may be used to compute them as will be shown in this chapter.

V.1 Pressure Distribution

Pressure drop in the heat exchanger can be computed with the use of the velocity field obtained in the numerical solution. However, because of the geometric irregularity of the exchanger, there is a lack of a common axis along which this pressure drop can be evaluated all the way from inlet to exit. The centerline of the pipes, which is commonly used as a basis for evaluating the pressure drop in pipe-flow problems, is not suited for use in the present investigation because it terminates at the center of the end cap. The inner pipe wall, fortunately, has a continuous contour all the way from the inlet to exit; it is thus used as a basis for evaluating the pressure drop.

The Navier-Stokes equations can be used together with the continuity equation and vorticity to derive the dimensionless pressure gradients at the wall as (Appendix D)

$$\frac{\partial p}{\partial z} = - \frac{1}{\text{Re}} \left(\frac{1}{r} \frac{\partial r \Omega}{\partial r} \right) \quad (5.1)$$

and

$$\frac{\partial p}{\partial r} = \frac{1}{\text{Re}} \frac{\partial \Omega}{\partial z} \quad (5.2)$$

where

$$p = p^* / (\rho u_m^{*2}) \quad (5.3)$$

Since only the total pressure drop and the pressure gradient along the wall are of concern, pressure at exit is assigned to be zero,

$$p_{\text{ex}} = 0 \quad (5.4)$$

This eliminates the need for determination of an arbitrary constant when the pressure drop is found later.

A refinement is made by defining a new dimensionless pressure so that the flow characteristics of both Poiseuille flow and annular flow may be incorporated. Notice that, for a fully developed flow in an annulus [17]

$$\frac{\text{Re}}{(8/C^+)} \frac{dp_{fd}}{dz} = -1 \quad (5.5)$$

In this equation,

$$C^+ = r_0^2 \left[(1+r^{+2}) - \frac{1-r^{+2}}{\ln(1/r^+)} \right] \quad (5.6)$$

and p_{fd} is dimensionless, $p_{fd} = p_{fd}^* / (\rho u_m^{*2})$; Re is the Reynolds number; r^+ in Eq. (5.6) is a radius ratio, $r^+ = r_{i0}^* / r_o^*$.

For a Poiseuille flow under a fully developed condition, Eq. (5.5) is changed to

$$\frac{Re}{8} \frac{dp_{fd}}{dz} = -1 \quad (5.7)$$

which can be recast as

$$\frac{Re}{(8/C^+)} \frac{dp_{fd}}{dz} = -C^+ \quad (5.8)$$

Comparing Eqs. (5.5) and (5.8) provides a clue for a new pressure defined as

$$p^+ = \frac{Re}{(8/C^+)} p \quad (5.9)$$

With this definition, the pressure gradients at the inner wall become

$$\frac{\partial p^+}{\partial z} = - \frac{1}{8/C^+} \left(\frac{1}{r} \frac{\partial r \Omega}{\partial r} \right) \quad (5.10)$$

and

$$\frac{\partial p^+}{\partial r} = \frac{1}{(8/C^+)} \frac{\partial \Omega}{\partial z} \quad (5.11)$$

Correspondingly, the exit pressure condition should satisfy

$$p_{ex}^+ = 0 \quad (5.12)$$

following Eq. (5.4).

It is also noted that, in the solution of the flow field, the flow quantities have been assumed to be invariant in the z direction. It follows that

$$\frac{dp_{ex}^+}{dz} = \frac{dp_{fd}^+}{dz} = -1 \quad (5.13)$$

must be met.

The formulation given above completes the preparation of evaluating the pressure drop whose derivation will now follow.

Along the inner pipe wall of the exchanger, the pressure drop can be evaluated using a line integral

$$\Delta p^+ = p_2^+ - p_1^+ = \int_{t_1}^{t_2} \frac{\partial p^+}{\partial t} dt \quad (5.14)$$

where t refers to a surface coordinate. The integrand in this equation can be expressed by means of a vector analysis as

$$\frac{\partial p^+}{\partial t} = \nabla p^+ \cdot \hat{t} = \left(\frac{\partial p^+}{\partial z} \hat{e}_z + \frac{\partial p^+}{\partial r} \hat{e}_r \right) \cdot \hat{t} \quad (5.15)$$

where \hat{t} is a unit vector tangential to the wall. Expressions for $\partial p^+/\partial z$ and $\partial p^+/\partial r$ have been given previously as Eqs. (5.10) and (5.11). In the transformed plane, they become (Appendix A)

$$\frac{\partial p^+}{\partial z} = - \frac{1}{(8/C^+)} \frac{1}{r} \frac{z_\xi (r\Omega)_\eta - z_\eta (r\Omega)_\xi}{J} \quad (5.16)$$

and

$$\frac{\partial p^+}{\partial r} = \frac{1}{(8/C^+)} \frac{r_\eta \Omega_\xi - r_\xi \Omega_\eta}{J} \quad (5.17)$$

Notice that, in the transformed plane, the inner wall corresponds to lines of constant η . The unit tangential vector \hat{t} in Eq. (5.15) thus takes the following form (Appendix A):

$$\hat{t} = \frac{z_\xi \hat{e}_z + r_\xi \hat{e}_r}{\sqrt{\gamma}} \quad (5.18)$$

The differential arc length along lines of constant η is

$$dt = \sqrt{\gamma} d\xi \quad (5.19)$$

Introducing Eqs. (5.15) through (5.19) into (5.14) gives

$$\begin{aligned} \Delta p^+ = p_2^+ - p_1^+ = & \\ & \int_{\xi_1}^{\xi_2} \left\{ - \left[\frac{1}{(\delta/C^+)} \frac{z_\xi(r\Omega)_n - z_n(r\Omega)_\xi}{rJ} \right] z_\xi \right. \\ & \left. + \left(\frac{1}{(\delta/C^+)} \frac{r_n \Omega_\xi - r_\xi \Omega_n}{J} \right) r_\xi \right\} d\xi \end{aligned} \quad (5.20)$$

which is to be integrated by using the trapezoidal rule.

V.2 Nusselt Number

The local Nusselt number along the inner wall can be evaluated using

$$Nu_z = \frac{hD_h}{k} = - \frac{C_h}{\theta_m} \left(\frac{\partial \theta}{\partial n} \right)_w = - \frac{C_h}{\theta_m} \left(\frac{\sqrt{\gamma} \theta_n}{J} \right)_w \quad (5.21)$$

where C_h is a dimensionless hydraulic diameter, defined as

$$C_h = D_h / r_i^* \quad (5.22)$$

D_h is the hydraulic diameter; θ_m in Eq. (5.21) denotes a mixing cup temperature, defined as [18]

$$\theta_m = \frac{\int_{r_1}^{r_2} u \theta r \, dr}{\int_{r_1}^{r_2} u r \, dr} \quad (5.23)$$

in the physical plane. This equation can be used directly to evaluate the mean temperature in domains B and C, figure 3, where the grid lines in both the physical and computational planes are orthogonal.

In domain A, the grid lines in the physical plane are oblique; to use Eq. (5.23) will require a cumbersome interpolation, which is inconvenient. For this reason, an alternative expression is used as follows:

$$\theta_{m2} = \theta_{m1} + \frac{2}{Pe} \int_{z_1}^{z_2} \frac{\partial \theta}{\partial n} r \, dz \quad (5.24)$$

This expression was derived based on an energy balance of the control volume shown in figure 8. Since only the inner wall is heated in the present exchanger, the r value in the integrand is taken to be unity when θ_{m2} is evaluated in the inner pipe. In the annulus, this value is taken to be 1.01 because of the dimensions of the inner pipe. Also notice that, in the computational plane, Eq. (5.24) reduces to

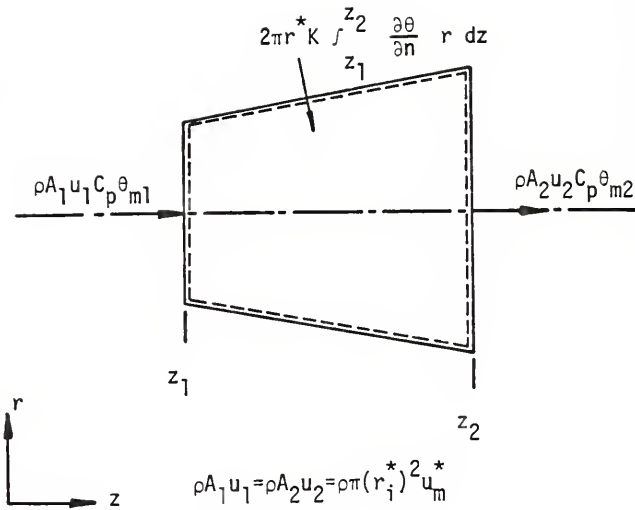


Figure 8 A Control Volume Used to Find the Mean Temperature by Energy Balance

$$\theta_{m2} = \theta_{m1} + \frac{2}{Pe} \int_{\xi_1}^{\xi_2} \frac{r}{J} \gamma \theta_n d\xi \quad (5.25)$$

The scheme developed above works well in the pipe regions where the flow sections are uniform. At the turning tip (point h, figure 3), no hydraulic diameter is defined. The characteristic length, C_h , at this point is thus arbitrarily taken to be twice of that length from the tip to the cap wall, that is, the dashed line in figure 2.

Once the local Nusselt number is found, the mean Nusselt number may be computed using

$$Nu_m = \frac{\int Nu_z dA}{\int dA} = \frac{\int Nu_z r dz}{\int r dz} \quad (5.26)$$

Further notice that, at the inlet section, the local Nusselt number is infinity because of the step change in temperature. In order to circumvent this problem while still evaluating a mean Nusselt number useful for the present investigation, the local Nusselt number at the inlet is estimated by extrapolating those numbers at two adjacent points, $i=2$ and 3 . The results are provided in the next chapter.

CHAPTER VI RESULTS AND DISCUSSION

Numerical results for the velocity field, temperature field, wall vorticity, pressure, and Nusselt number will be presented in this chapter for Reynolds numbers of 100, 500, and 1000 and Prandtl numbers of 0.7, 20, and 100. Computation was performed on a Harris 800 computer, and machine plots were executed with the use of a Gould plot-routine package.

VI.1 Velocity Field

Velocity fields for three Reynolds numbers are presented in figure 9. Enlarged views of the velocity fields near the turning point of the inner pipe are provided in figures 10 through 12. In making these plots, all arrow heads of the velocity vectors are positioned along lines that correspond to lines of constant ξ in the computational plane. Hence, these arrow heads do not line up radially when they move closer to the turning point because they are in domain A (figure 3) and in this domain these constant ξ lines are oblique in the physical plane, also see figure 4. Certainly, the lengths of the arrows still represent the magnitude of the velocity. It is also

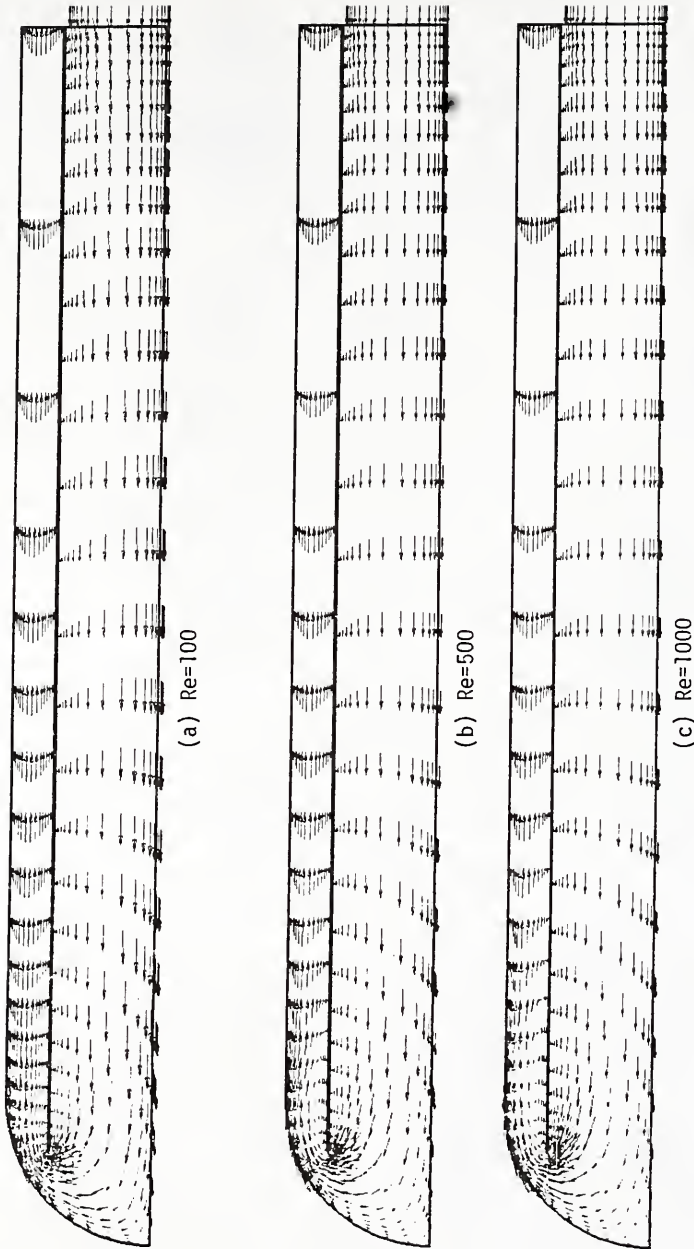


Figure 9 Velocity Fields for Re=100, 500, and 1000

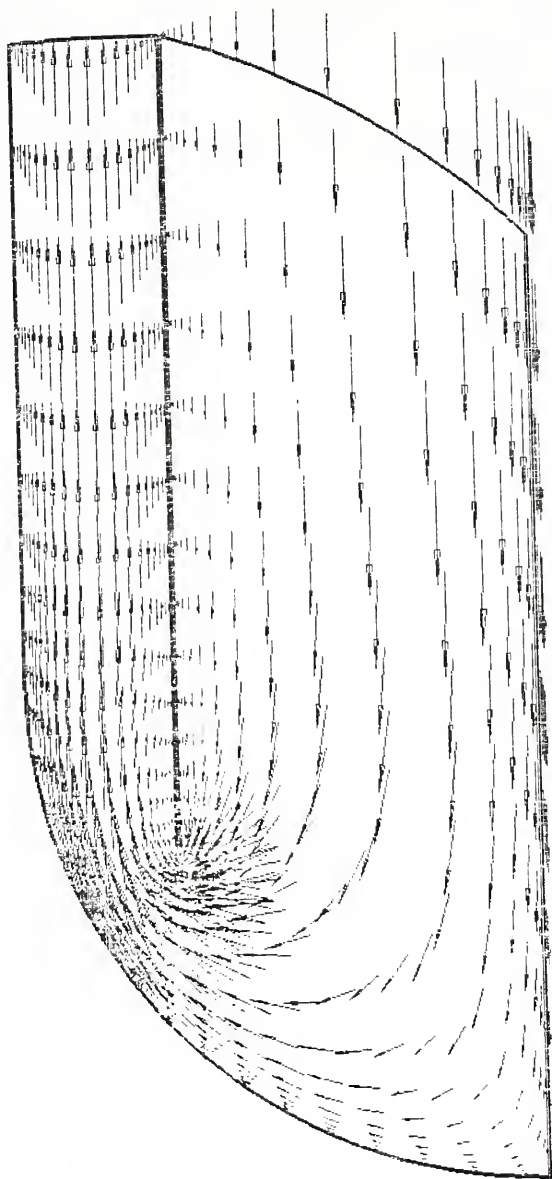


Figure 10 Velocity Field Near Turning Point for $Re=100$

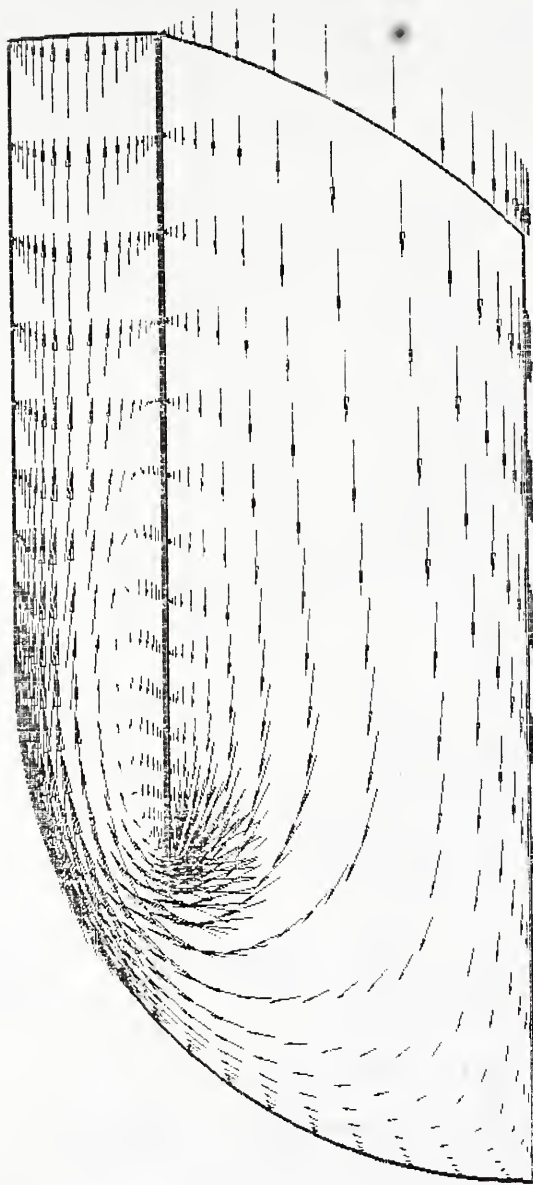


Figure 11 Velocity Field Near Turning Point for $Re=500$

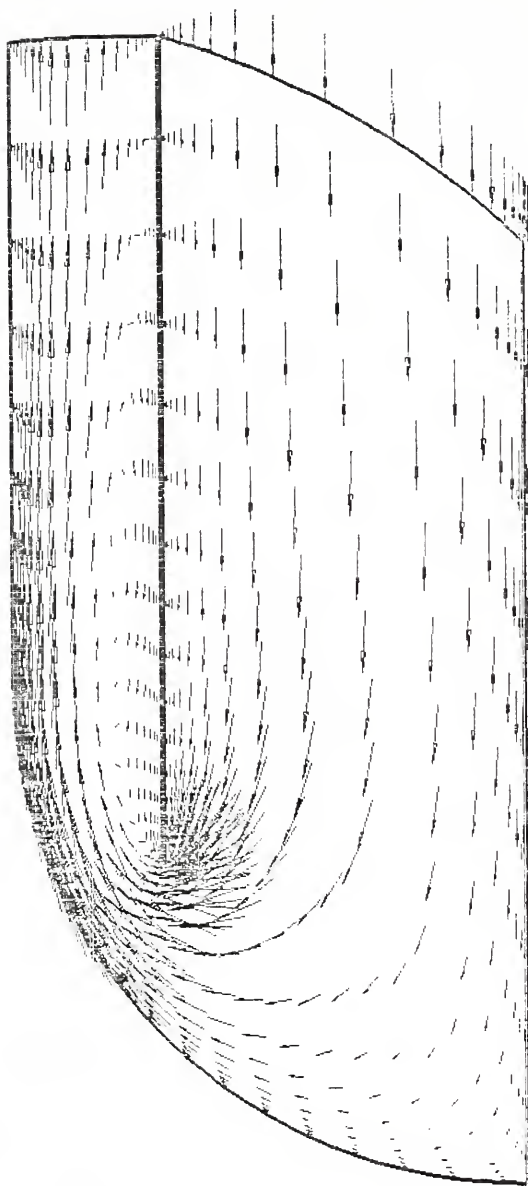


Figure 12 Velocity Field Near Turning Point for $Re=1000$

noted that, in making these plots, the magnitude of the velocity has been normalized by the maximum velocity found for each Reynolds number tested. Inasmuch as the maximum velocity for $Re=1000$ is larger, the normalized velocities in this plot are smaller.

A close examination of the computer data shows that, immediately following the flow entering the inner pipe, there is a slight bulge of the velocity near the inner pipe wall (too small to be seen clearly in figure 9). The fluid velocity near the centerline, however, remains uniform at its inlet value. Such an observation appears to be in contradiction to the developing flow analyses in which such a bulge is not reported. This inconsistency may be ascribed to the fact that, in the present investigation, the axial shear term in the momentum equation is retained in the computation, whereas in the developing flow analyses, references [18] and [19], such axial shear terms are dropped. Physically, this bulge of velocity results from the need for flow to satisfy the continuity equation and the no-slip condition simultaneously. Because of the closeness of this section to the inlet, the momentum transfer has yet to reach that far to the center region, and as a result, only velocity nearby is affected and a maximum velocity develops locally. Such a phenomenon has also been discussed in references [20] and [21].

A vortex is found in the annulus right after the flow makes the 180-degree turn. As shown in figures 10 through 12, the size of the recirculation zone increases with Reynolds number. For a quantification of this observation, the sizes of the vortex measured in distance from the turning point to the point of flow reattachment are listed in Table 1. With the recirculation region, fluid moves in a clockwise loop. The main flow detaches from the wall, resulting in a depression of the heat transfer rate as will be discussed later.

It is also interesting to note that, because of the blockage of flow by the round cap, the maximum velocity in the inner pipe is not located on its centerline, but at a location slightly shifted away from the center. By the same token, the maximum velocity in the annulus is not located close to the inner wall, as is normally the case for an annular flow [17], but is displaced slightly toward the outer wall. This latter phenomenon is certainly a result of the accelerated main flow that occurs near the recirculation region being displaced away from the inner wall.

VI.2 Wall Vorticity

The vorticity along the inner pipe wall is plotted as a function of position (dimensionless) in figure 13. The turning point of the inner pipe is located at 0.5; the

Table 1

Vortex Sizes for $Re=100, 500, \text{ and } 1000$

Reynolds Number	Vortex Size
100	0.37
500	1.37
1000	2.3

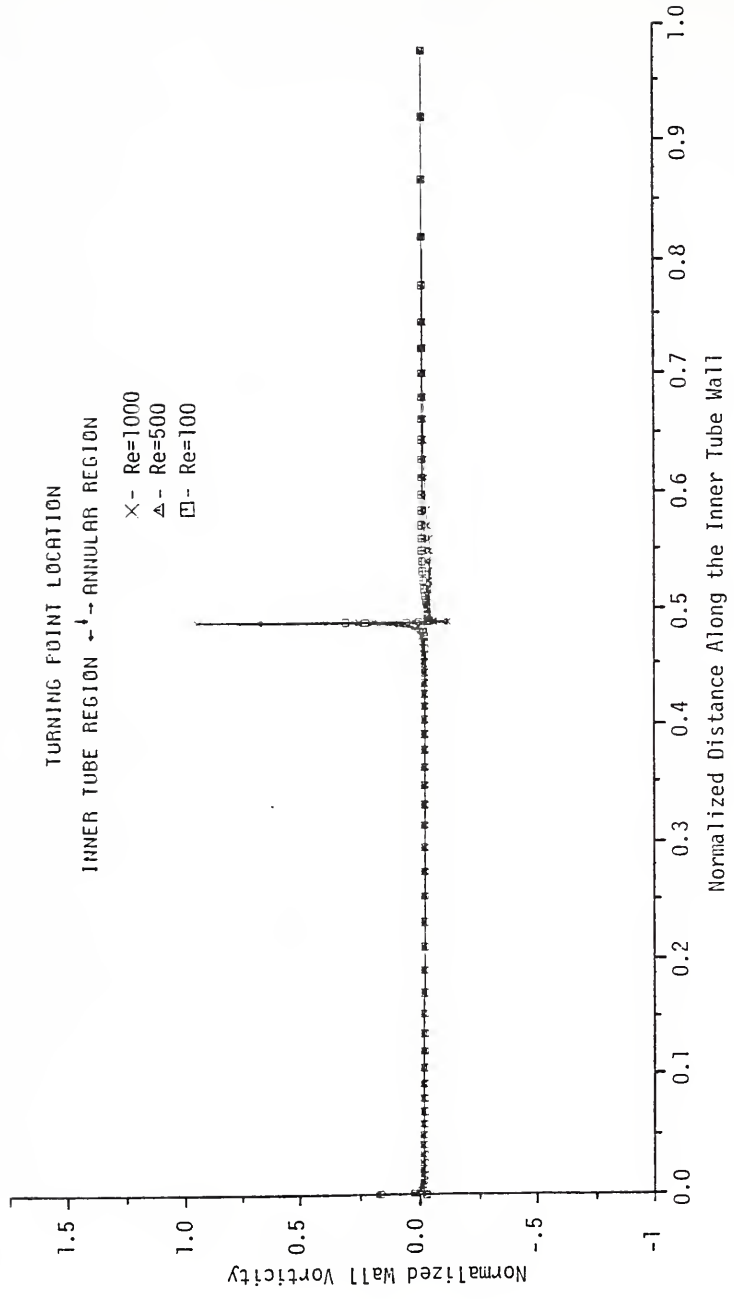


Figure 13 Vorticity on the Inner Wall

normalized overall length is 1. Again, the vorticity is dimensionless, normalized by the maximum vorticity value (786.105) found for the three cases of Reynolds number tested.

There are three places where the vorticity shows a deviation: the inlet region, the flow region near the turning point, and the flow in the recirculation region. The slight increase in vorticity in the inlet region can be attributed to the growth of the boundary layer under a no-slip condition. A larger vorticity in this region enables these conditions to be met. Moving downstream, the vorticity diffuses via random molecular motion and convection; the vorticity tends to flatten out as shown in the figure.

The turning point provides a different perspective. Here from mathematics, this point is a point of singularity, and the vorticity approaches infinity. Physically, the flow accelerates in the 180-degree turn, and correspondingly, the pressure drops as will be discussed later.

As shown in figure 13, the vorticity changes sign in the recirculation region, also see Table 2. Finally, as the fluid moves further downstream toward exit, three vorticity curves all merge into one.

Table 2
 Inner-Wall Vorticity Data Near the Turning Point

$i \backslash \Omega$ Re	100	500	1000
92	15.2166	40.7738	62.8808
93	19.4822	54.5176	84.0731
94	25.5662	74.6961	114.966
95	34.3638	105.127	161.401
96	47.5037	152.317	233.401
97	69.3520	227.864	346.933
98	114.130	351.229	513.606
99	210.448	572.942	786.105*
100	362.966	639.621	711.617
101**	278.764	244.890	180.865
102	152.656	1.12102	-47.3047
103	26.7717	-66.1383	-73.1212
104	-0.526885	-43.7028	-42.0327
105	-6.66565	-29.1544	-26.0498
106	-7.3296	-20.5753	-17.5287
107	-6.6902	-15.4656	-12.7805
108	-5.88388	-12.2948	-9.94225
109	-5.13125	-10.2201	-8.10281
110	-4.48652	-8.83588	-6.86040

* Maximum value

** Turning point

VI.3 Pressure on Inner Wall

The pressure distribution on the inner wall is plotted for the three Reynolds numbers in figure 14. Here the ordinate is a dimensionless pressure defined as Eq. (5.9); the x axis is again dimensionless as before. Three additional informations are included in the figure for contrast. Two of them correspond to the pressure drop for fully developed flow in a circular pipe and in an annulus, in which the pressure gradient is linear and is independent of the Reynolds number; see solid lines for Poiseuille flow and annular flow. This is certainly a result of the definition p^+ . Another set of results, which are plotted using the stars in the figure, is taken from the numerical work of Hornbeck [22] who evaluated the total pressure drop for a hydrodynamic developing flow in a circular pipe; again the slope of these data are in agreement with that calculated in the present exchanger. It should be noted that the level of these curves is arbitrary; only the pressure gradients are of concern. From the figure, it is clear that the pressure drop in the inner pipe in the present exchanger is only affected near the turning point. To assist this observation, a dashed line is drawn in the figure to indicate the approximate location where the pressure is affected in the inner-pipe region.

For the heat exchanger, there are three places where the pressure drop appears unusual. Right after the fluid

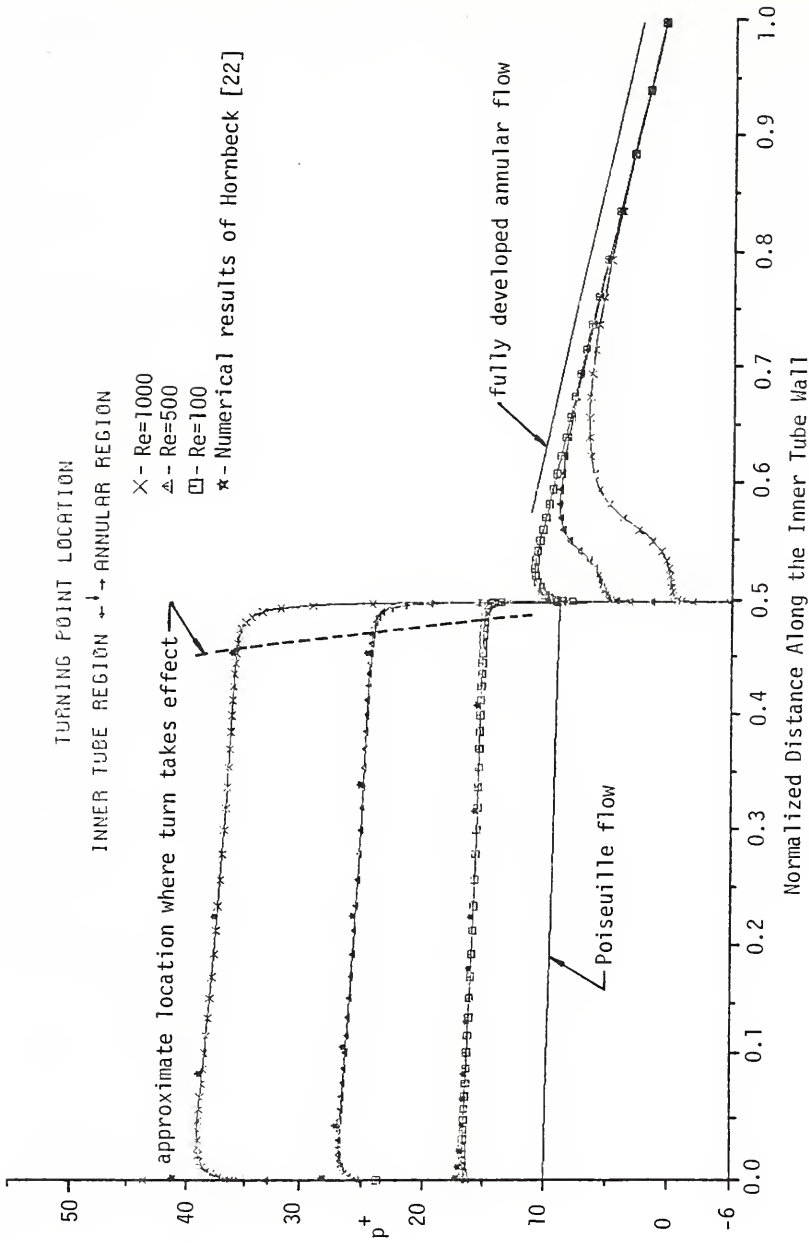


Figure 14 Pressure Distribution on the Inner Wall

enters the inner pipe, the pressure gradient is positive. This is not predicted in Hornbeck's results because, in his analysis, the axial boundary-layer equation was used and the momentum equation was linearized locally at any cross section z_1 by means of the velocity at $z=z_1+\Delta z$. However, in the present investigation, no linearization is made and the axial diffusion terms are retained in the momentum equations. As a result, this positive pressure gradient near the inlet region may be attributed to the inclusion of the axial diffusion terms in these equations. The requirement for satisfying the uniform flow boundary condition at inlet also contributes to this pressure rise. Notice that this pressure abnormality was also reported by Morihara and Cheng [20] for flow in a straight channel, and they used a similar mathematical model as used in the present study. A point of interest is that both the pressure rise and the distance over which it occurs are larger for larger Reynolds numbers, which is not unexpected.

Before the flow reaches the turning point on the inner wall, there is a rapid drop in pressure. Obviously, this drop results from acceleration occurring before the 180-degree turn (see dashed line). There is only partial recovery of this pressure as the fluid enters the annulus; as would be expected, the pressure loss is partially irreversible.

The circulation of flow in the annulus gives rise to another region of positive pressure gradient. Finally, all three curves merge toward the exit of the exchanger in satisfaction of the conditions imposed there, Eqs. (5.4) and (5.13). The flow becomes fully developed as evidenced by the solid line drawn in the figure. To test the accuracy of the pressure computed in the numerical work, dp_{ex}^+/dz is evaluated at the exit section. As listed in Table 3, this pressure gradient has a value ranging from -1.0245 to -1.0781; the error is thus about 8% as compared with the pressure gradient for annular in a fully developed condition; also see Eq. (5.13).

VI.4 Temperature Field

Isotherms are plotted in figures 15 through 17. Recall that, for the problems under investigation, $\theta=0$ along the inner wall, and $\theta_n=0$ along the outer wall. Notice that, each figure presents results for all three Reynolds numbers at one Prandtl number. Hence, comparison between the isotherm distributions of one figure provides insight into the effect of Reynolds number; a cross reference of the plots at the same Reynolds number offers an assessment of the effect of the Prandtl number.

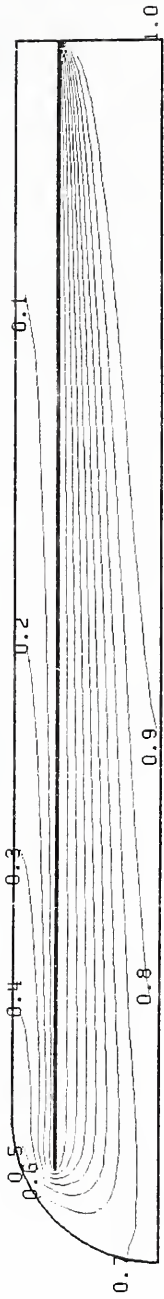
The boundary conditions required that all isotherms emerge from the junction of the inner wall with the inlet. When one compares any position downstream of the

Table 3

Dimensionless Pressure Gradients at Exit

Re	$\frac{dp}{dz}_{ex}^+ *$
100	-1.0245
500	-1.0781
1000	-1.0687

* Correct value: -1



(a) Re=100

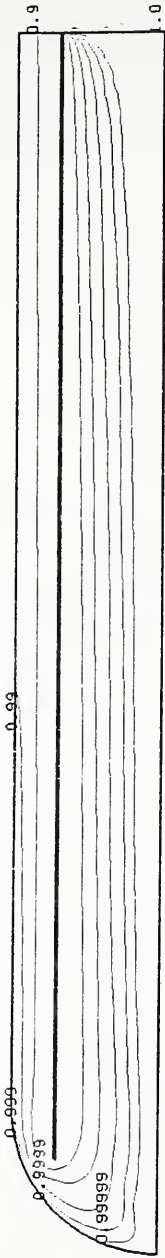


(b) Re=500



(c) Re=1000

Figure 15 Isotherms for $Pr=0.7$ and $Re=100, 500,$ and 1000



(a) Re=100



(b) Re=500

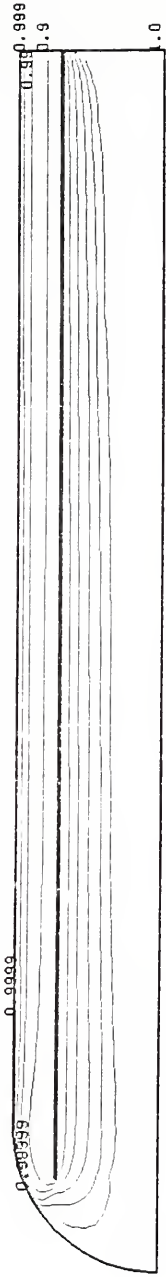


(c) Re=1000

Figure 16 Isotherms for Pr=20 and Re=100, 500, and 1000



(a) Re=100



(b) Re=500



(c) Re=1000

Figure 17 Isotherms for Pr=100 and Re=100, 500, and 1000

entrance, it is observed that an increase in Reynolds number at the same Prandtl number produces a steeper temperature gradient near the (inner) wall.

A cross reference of the plots in the three figures at fixed Reynolds number reveals that an increase in the Prandtl number produces the same general effect as an increase in Reynolds numbers. This is to be expected since increased Prandtl number implicates a smaller thermal diffusion as compared to the momentum diffusion. Therefore, heat entering the fluid at the inner wall is unable to penetrate as deeply into the fluid. In fact, figure 16 (a) shows these isotherms are so crowded near the wall that full presentation of them becomes impossible; only those isotherms from 0.9 to 0.99999 are thus shown.

For all cases tested, the isotherms are crowded toward the turning point of the inner pipe. This results from the high velocity in this region. With respect to the large wall gradients isotherms observed near the inlet section and near the turning point, it should be noted that these imply high convective coefficients in these regions.

A totally different state of affairs occurs in the recirculation region following the sharp turn. Figure 15 (b) and (c) show a smaller temperature gradient in these regions, indicating a lower heat transfer coefficient.

Further downstream where the fluid reattaches to the wall, a crowding of the isotherms; see figure 15 (b) and (c), indicates slight rise of the convective coefficient.

These observations are summarized in a series of Nusselt-number plots presented in the next section.

VI.5 Local Nusselt Number

Local Nusselt numbers for the nine cases are shown in figures 18 through 20 at three Prandtl numbers. Two pieces of information are also included in figure 18; one relates to the Nusselt number for fully developed flow in a circular pipe under a constant-wall-temperature condition. The Nusselt number for this case is 3.658 [18]; see horizontal line drawn. The other set of data is taken from the numerical work of Hornbeck [23] who studied the Nusselt number under a developing flow and heat transfer condition at the same Prandtl number (0.7). His results are plotted using stars in the figure.

Referring to figure 18, it is seen that the present Nu_2 values are in good agreement with the results of Hornbeck for $Re=100$. Moving downstream, the local Nusselt numbers asymptotically approach those for fully developed flow. Near the turning point, the turn takes effect, resulting in an increase in heat transfer and the local Nusselt numbers increase rapidly. Again, to assist this observation, a dashed line is drawn in this figure to

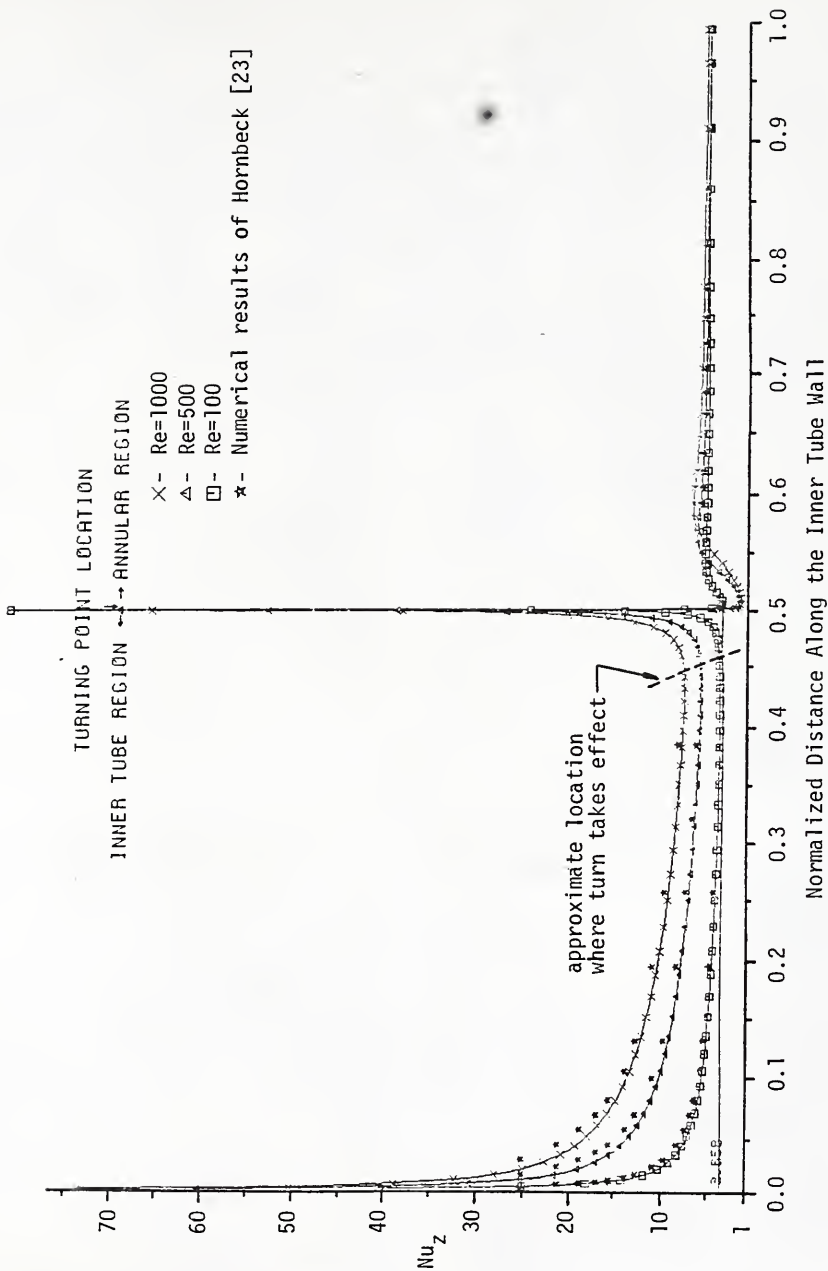


Figure 18 Local Nusselt Number for $Pr=0.7$ and $Re=100, 500, \text{ and } 1000$

indicate the approximate location where turn takes effect. For the higher Reynolds number case, the local Nusselt numbers near the inlet region of the present study deviate only slightly from the Hornbeck's results.

For all the cases studied for the heat exchanger, a large Nusselt number is found near the inlet, the turning point, and in the reattachment region and low Nusselt number occurs in the recirculation region.

It is clear that once the flow is deflected into the annulus, a redevelopment of flow occurs. In the annulus region, a fully developed condition is reached earlier for fluid of low Peclet number, see figures 18 through 20. In order to check on the computations of the present work, Lundberg and coauthors' results [24] are used. As shown in Table 4, Lundberg's results for fully developed velocity and temperature profiles in an annulus appear to be in good agreement with the present investigation that is computed at $Pr=0.7$ and $Re=100$. If a linear interpolation based on Lundberg's results at $r^+=0.5$ and 1.0 can serve as a guide, then the error is only 1.3%.

VI.6 Mean Nusselt Number

Figure 21 presents mean Nusselt number as a function of Reynolds number with Prandtl number as a parameter. This figure shows that mean Nusselt number increases with both the Reynolds and Prandtl numbers. A correlation of

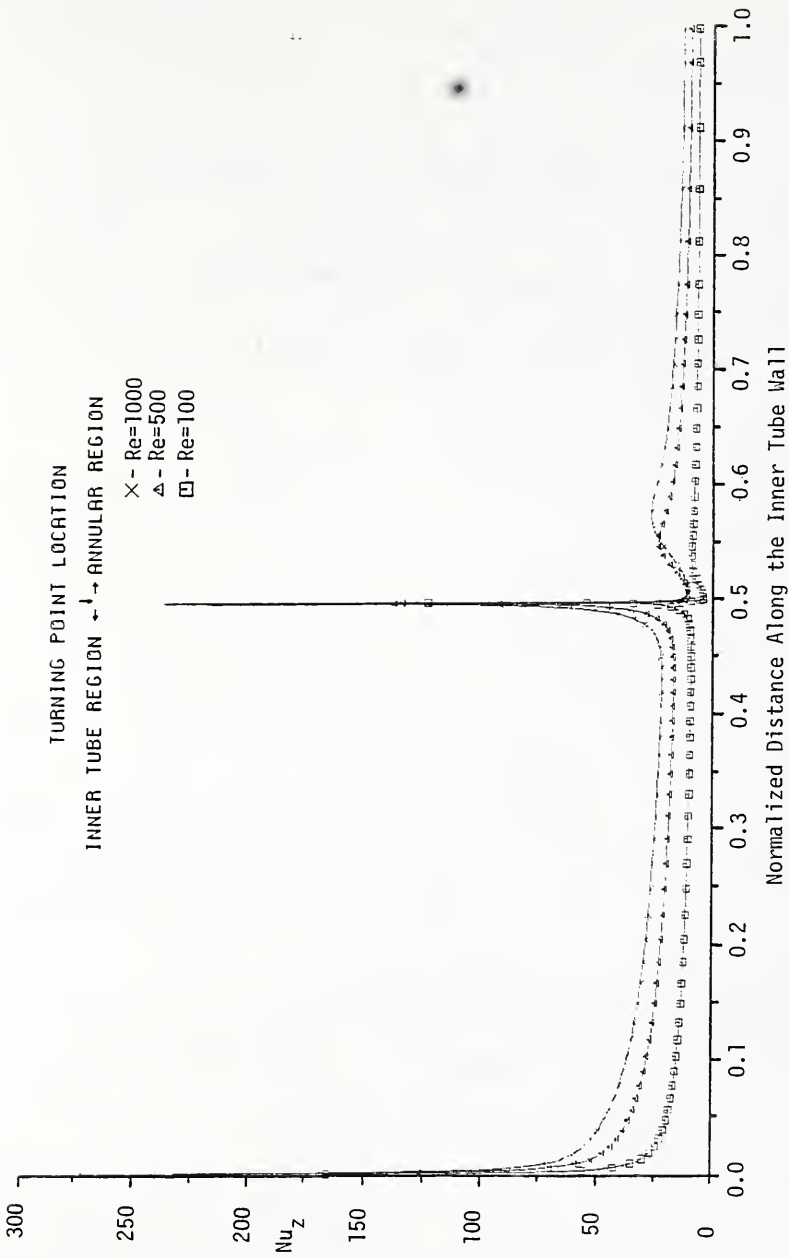


Figure 19 Local Nusselt Number for $Pr=20$ and $Re=100, 500, \text{ and } 1000$

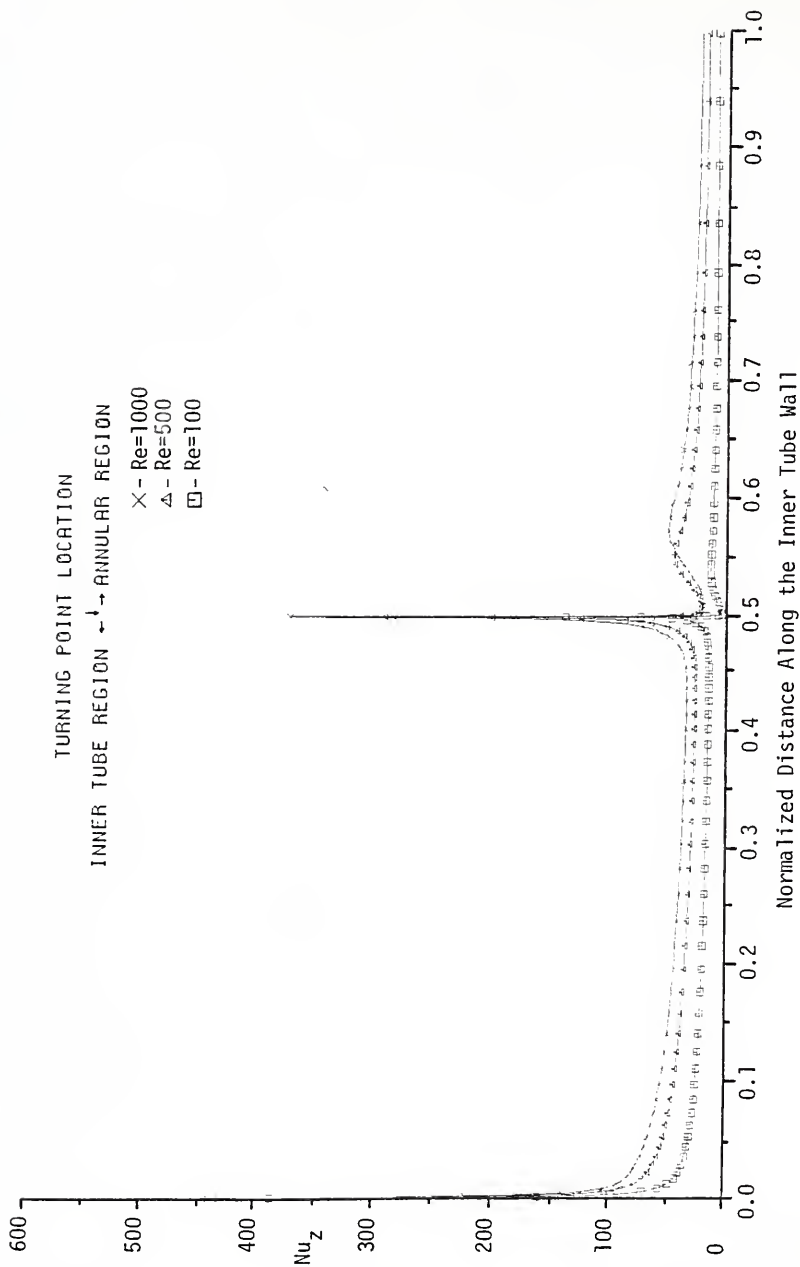


Figure 20 Local Nusselt Number for $Pr=100$ and $Re=100, 500,$ and 1000

Table 4

Comparison of the Computed Local Nusselt Number
at the Exit with Lundberg's Data

r^+	Nusselt Number
0.5*	5.738
0.711**	5.297
1.0*	4.861

* Lundberg's data

** Present investigation for $Pr=0.7$ and
 $Re=100$

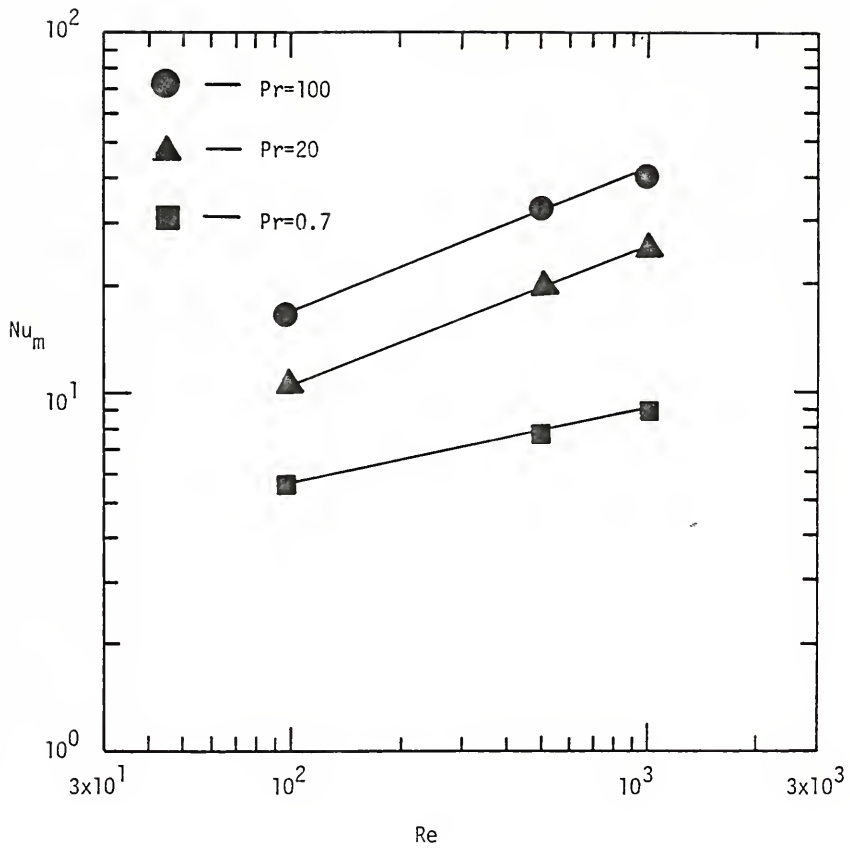


Figure 21 A Plot of Mean Nusselt Number

the results yields

$$\text{Nu}_m = 1.15 \text{Re}^{0.328} \text{Pr}^{0.268} \quad (6.1)$$

which is valid for $\text{Re}=100$ to 1000 , and $\text{Pr}=0.7$ to 100 . Variance evaluated based on $(n-2)$ degree of freedom (n represents number of correlated point) is 2.6 [25].

The present heat exchanger is found to be far more effective in heat transfer. To verify this point, Hornbeck's data [23] for air ($\text{Pr}=0.7$) under a developing velocity and temperature condition in a circular pipe are used for comparison. As listed in Table 5, the mean Nusselt number for the SPRF heat exchanger is 1.57 times that for pipe flow when the Reynolds number is 500 . Doubling this Reynolds number enables this Nusselt-number ratio to be raised to 1.87 . The superiority of the present exchanger is thus clearly seen.

VI.7 Truncation Error and Convergence

In order to check the truncation error and the convergence of the solutions presented, three different grid systems are used. It is noted that, for the ease of comparison, the number of grid points along the constant n -line is fixed at 163 ; the number of grid points along the constant ξ -line is tested for 21 , 41 , and 61 . This results in lines of constant ξ for these grid systems having the

Table 5

Comparison of Mean Nusselt Number Between
SPRF Heat Exchanger and Heating in a Circular Pipe

Pr	Re	Mean Nusselt Number		Mean Nusselt- Number Ratio
		Hornbeck's Data*	Present Study	
0.7	500	7.4	11.62	1.57
0.7	1000	9.57	17.88	1.87

* Developing velocity and temperature profiles in a circular pipe

same contours in the physical plane but with different grid sizes.

Figure 22 shows the computed stream functions along constant ξ -lines for the three grid systems. In these figures, $i=50$ and 152 correspond to the mid-section in the inner pipe and the annular region, respectively; $i=101$ corresponds to the constant ξ -line at the turning point (see figure 5). It is clear that the computed stream function values based on the use of grids 163×41 converge to the results of the dense grid (163×61). A close examination of the difference between these two sets of data shows that the maximum deviation is only about 3% relative to the dense grid. However, the CPU time required for computation with the dense grid is increased by a factor of about 3.5 (Table 6) using the Harris 800 computer on campus. For this reason, a denser grid is not used for the present computation. The results for 163×41 are considered converged.

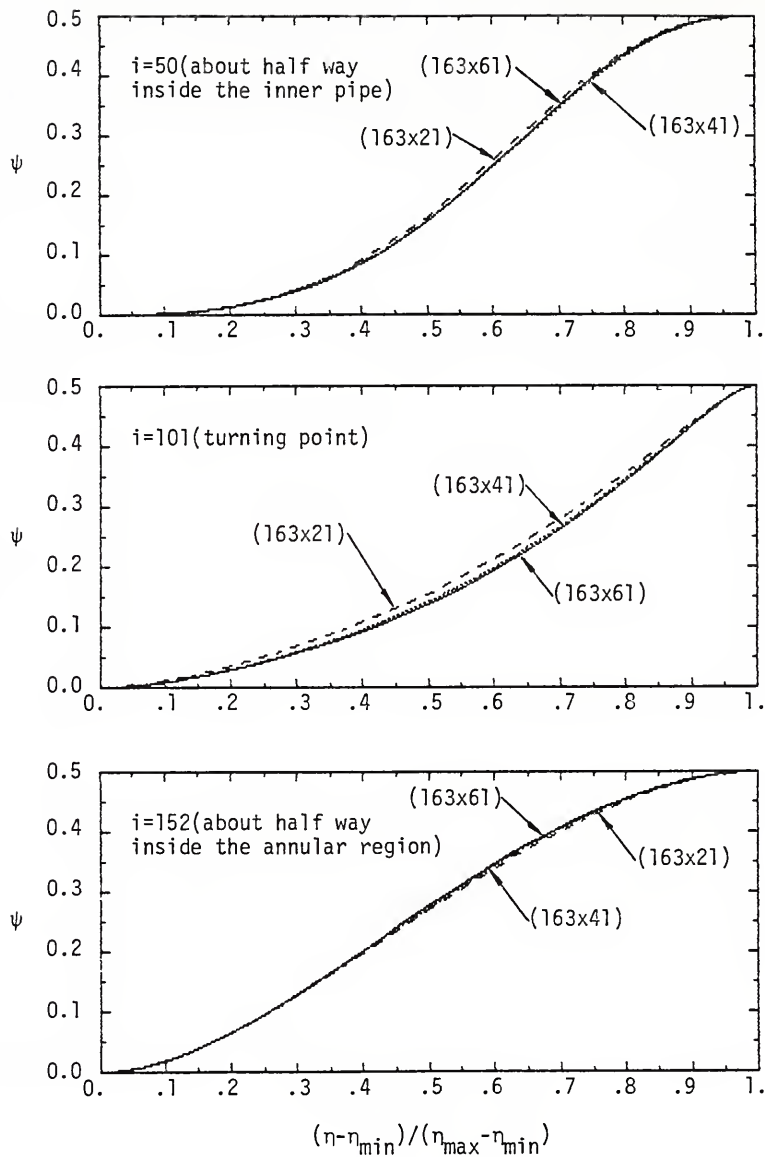


Figure 22 Comparison of the Computed Stream Functions Along Constant ξ -line for Different Grid Systems

Table 6

CPU Time Required for Computation of
Stream Functions Given in Figure 22

Grids	Re		
	100	500	1000
163x21	1 hr 30 min	57 min	1 hr 17 min
163x41	4 hr 55 min	4 hr 14 min	6 hr 19 min
163x61	12 hr 15 min	10 hr 3 min	18 hr 16 min

* CPU time is based on the use of Harris 800
computer on campus

CHAPTER VII CONCLUSIONS AND RECOMMENDATIONS

A numerical solution is given for studying the flow and heat transfer in a single-pass, return-flow heat exchanger. Stream function and vorticity are used in the formulation, and the original irregular geometry of the exchanger in the physical plane is transformed into a rectangular domain with square grids in a computational plane. Elliptic partial differential equations are used in the transformation, and grid lines are clustered with the use of separate clustering functions which allow fine grids to be formed in regions where the flow and temperature fields change most rapidly. The source terms in the Poisson's equations are also evaluated in the solution.

A finite difference method is used to solve the problem in the computational plane. In the numerical algorithm, in order to assure a convergent solution in the iteration, the diagonal terms in the resulting matrix equations are reconstructed to make them dominant. Vorticity boundary conditions at the walls are expressed in a first-order approximation. The velocity and temperature conditions along the centerline of the heat exchanger are also finite differenced, with the first-order differential

terms of velocity and temperature expressed in a first-order approximation. Solutions are obtained for $Pr=0.7$, 20, and 100, and $Re=100$, 500, and 1000.

Numerical data show a marked increase in velocity as flow makes a 180-degree turn in the end cap. Here a rapid drop of pressure is also noticed. Once the flow enters annulus, the main flow is separated from the inner wall, and a recirculation is found near the wall. This results in a drop in the heat transfer coefficient in this recirculation region. Moving further downstream, the flow reattaches to the wall, causing a slight rise in the heat transfer. The mean heat transfer coefficient for the heat exchanger is found to be proportional to the Reynolds number and Prandtl number. The numerical results are correlated to develop an empirical equation.

For a check of the accuracy in the solution, the pressure gradient and the Nusselt number at the exit of the exchanger are also evaluated and compared with the theory (analytical equation) and practice (literature data). The agreement is satisfactory. The single-pass, return-flow heat exchanger is found to have a mean Nusselt number that is about 1.57 to 1.87 times that for heat transfer in a singular pipe under comparable working conditions ($Pr=0.7$, and $Re=500$, and 1000). The exchanger is thus shown to be effective in heat transfer.

Based on the study made in this dissertation, directions of further research are charted as follows.

1. There are a wide range of variations in the conditions used which the SPRF exchanger can be operated. They include (i) change in the flow direction, (ii) change in the system geometry, particularly that gap size from the inner pipe to the end cap, (iii) change in thermal boundary conditions on both walls, and (iv) introducing minor modifications in the construction of the exchanger, such as eccentricity in the pipe layout, flow perturbation devices, etc. They provide a wide range of conditions to be tested in the future.
2. Because of the complexity of the geometry of the exchanger, it provides an opportunity for testing various numerical methods, particularly those approximation methods in the finite-difference formulation of the boundary conditions.
3. A study is not complete without experiment. It is highly desirable that hardware be built to test the results obtained in the numerical solution. A limited experimental program serves well to validate the numerical solution; until then the numerical solution can be used with confidence for acquiring data for various operating conditions.

APPENDIX A
DERIVATION OF TRANSFORMATION RELATIONS,
GOVERNING EQUATIONS, AND BOUNDARY CONDITIONS
IN THE TRANSFORMED PLANE

This appendix gives the derivation of the transformation relations, governing equations, and boundary conditions in the physical and computational planes when elliptic partial differential equations are used to generate the computational grid system.

Referring to figure A.1, the independent variables in the physical plane are $z(\xi, \eta)$ and $r(\xi, \eta)$, while those in the computational plane are $\xi(z, r)$ and $\eta(z, r)$. In the computational plane, the domain of interest is rectangular in shape and grids in this plane are uniformly spaced (i.e., square grid). Since all the computations are to be made in the transformed domain, the independent variables in the governing equations and boundary conditions must be changed from the physical domain to the transformed domain.

Consider the vector

$$\begin{bmatrix} z \\ r \end{bmatrix} = \begin{bmatrix} z(\xi, \eta) \\ r(\xi, \eta) \end{bmatrix} \quad (\text{A.1})$$

which may be differentiated to give

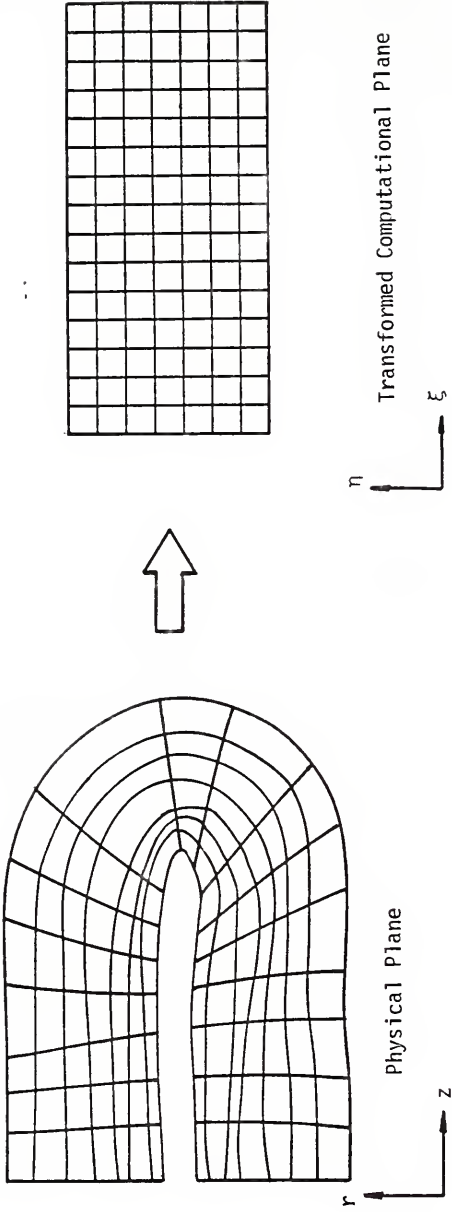


Figure A.1 Schematic Showing Transformation from Physical to Transformed Plane

$$\begin{bmatrix} dz \\ dr \end{bmatrix} = \begin{bmatrix} z_{\xi} & z_{\eta} \\ r_{\xi} & r_{\eta} \end{bmatrix} \begin{bmatrix} d\xi \\ d\eta \end{bmatrix} \quad (\text{A.2})$$

Cramer's rule may be used to solve for $d\xi$ and $d\eta$ as

$$\begin{bmatrix} d\xi \\ d\eta \end{bmatrix} = \frac{1}{J} \begin{bmatrix} r_{\eta} & -z_{\eta} \\ -r_{\xi} & z_{\xi} \end{bmatrix} \begin{bmatrix} dz \\ dr \end{bmatrix} \quad (\text{A.3})$$

where J is the transformation Jacobian

$$J = \frac{\partial(z, r)}{\partial(\xi, \eta)} = \begin{vmatrix} z_{\xi} & z_{\eta} \\ r_{\xi} & r_{\eta} \end{vmatrix}$$

Similarly,

$$\begin{bmatrix} d\xi \\ d\eta \end{bmatrix} = \begin{bmatrix} \xi_z & \xi_r \\ \eta_z & \eta_r \end{bmatrix} \begin{bmatrix} dz \\ dr \end{bmatrix} \quad (\text{A.4})$$

The following identities may be established by comparing (A.3) and (A.4)

$$\begin{aligned} \xi_z &= r_{\eta}/J \\ \xi_r &= -z_{\eta}/J \\ \eta_z &= -r_{\xi}/J \end{aligned} \quad (\text{A.5})$$

and

$$\eta_r = z_{\xi}/J$$

The original partial differentials in the physical plane may be transformed to the computational plane by using the chain rule for partial derivatives. It follows that

$$\begin{aligned}\frac{\partial}{\partial z} &= \xi_z \frac{\partial}{\partial \xi} + \eta_z \frac{\partial}{\partial \eta} \\ &= (r_\eta \frac{\partial}{\partial \xi} - r_\xi \frac{\partial}{\partial \eta})/J\end{aligned}\quad (\text{A.6})$$

$$\begin{aligned}\frac{\partial}{\partial r} &= \xi_r \frac{\partial}{\partial \xi} + \eta_r \frac{\partial}{\partial \eta} \\ &= (-z_\eta \frac{\partial}{\partial \xi} + z_\xi \frac{\partial}{\partial \eta})/J\end{aligned}\quad (\text{A.7})$$

$$\begin{aligned}\frac{\partial^2}{\partial z^2} &= \frac{\partial}{\partial z} \left(\xi_z \frac{\partial}{\partial \xi} + \eta_z \frac{\partial}{\partial \eta} \right) \\ &= \xi_{zz} \frac{\partial}{\partial \xi} + \xi_z \frac{\partial}{\partial z} \left(\frac{\partial}{\partial \xi} \right) + \eta_{zz} \frac{\partial}{\partial \eta} + \eta_z \frac{\partial}{\partial z} \left(\frac{\partial}{\partial \eta} \right) \\ &= \xi_{zz} \frac{\partial}{\partial \xi} + \xi_z \left[\left(\xi_z \frac{\partial}{\partial \xi} + \eta_z \frac{\partial}{\partial \eta} \right) \frac{\partial}{\partial \xi} \right] \\ &\quad + \eta_{zz} \frac{\partial}{\partial \eta} + \eta_z \left[\left(\xi_z \frac{\partial}{\partial \xi} + \eta_z \frac{\partial}{\partial \eta} \right) \frac{\partial}{\partial \eta} \right] \\ &= \xi_{zz} \frac{\partial}{\partial \xi} + \xi_z^2 \frac{\partial^2}{\partial \xi^2} + \eta_{zz} \frac{\partial}{\partial \eta} + \eta_z^2 \frac{\partial^2}{\partial \eta^2} \\ &\quad + 2 \xi_z \eta_z \frac{\partial^2}{\partial \xi \partial \eta}\end{aligned}\quad (\text{A.8})$$

and

$$\begin{aligned} \frac{\partial^2}{\partial r^2} = & \xi_{rr} \frac{\partial}{\partial \xi} + \xi_r^2 \frac{\partial^2}{\partial \xi^2} + \eta_{rr} \frac{\partial}{\partial \eta} + \eta_r^2 \frac{\partial^2}{\partial \eta^2} \\ & + 2 \xi_r \eta_r \frac{\partial^2}{\partial \xi \partial \eta} \end{aligned} \quad (\text{A.9})$$

Combining (A.8) and (A.9) gives the Laplace operator

$$\begin{aligned} \frac{\partial^2}{\partial z^2} + \frac{\partial^2}{\partial r^2} = & (\xi_z^2 + \xi_r^2) \frac{\partial^2}{\partial \xi^2} + 2(\xi_z \eta_z + \xi_r \eta_r) \frac{\partial^2}{\partial \xi \partial \eta} \\ & + (\eta_z^2 + \eta_r^2) \frac{\partial^2}{\partial \eta^2} + (\xi_{zz} + \xi_{rr}) \frac{\partial}{\partial \xi} \\ & + (\eta_{zz} + \eta_{rr}) \frac{\partial}{\partial \eta} \end{aligned} \quad (\text{A.10})$$

in which the coefficients for partial differentials on the right-hand side may be expressed in terms of J as

$$\xi_z^2 + \xi_r^2 = (z_\eta^2 + r_\eta^2)/J^2 = \alpha/J^2$$

$$\xi_z \eta_z + \xi_r \eta_r = - (r_\xi r_\eta + z_\xi z_\eta)/J^2 = -\beta/J^2$$

and

$$\eta_z^2 + \eta_r^2 = (z_\xi^2 + r_\xi^2)/J^2 = \gamma/J^2$$

where

$$\alpha = z_\eta^2 + r_\eta^2$$

$$\beta = r_\xi r_\eta + z_\xi z_\eta$$

$$\gamma = z_{\xi}^2 + r_{\xi}^2$$

Then,

$$\begin{aligned} \frac{\partial^2}{\partial z^2} + \frac{\partial^2}{\partial r^2} = \frac{1}{J} \left(\alpha \frac{\partial^2}{\partial \xi^2} - 2\beta \frac{\partial^2}{\partial \xi \partial \eta} + \gamma \frac{\partial^2}{\partial \eta^2} \right) \\ + (\xi_{zz} + \xi_{rr}) \frac{\partial}{\partial \xi} + (\eta_{zz} + \eta_{rr}) \frac{\partial}{\partial \eta} \end{aligned} \quad (\text{A.11})$$

If Laplace equations

$$\xi_{zz} + \xi_{rr} = 0 \quad (\text{A.12})$$

and

$$\eta_{zz} + \eta_{rr} = 0 \quad (\text{A.13})$$

are used in the transformation, Eq. (A.11) may be simplified to be

$$\frac{\partial^2}{\partial z^2} + \frac{\partial^2}{\partial r^2} = \frac{1}{J^2} \left(\alpha \frac{\partial^2}{\partial \xi^2} - 2\beta \frac{\partial^2}{\partial \xi \partial \eta} + \gamma \frac{\partial^2}{\partial \eta^2} \right) \quad (\text{A.14})$$

If Poisson equations

$$\xi_{zz} + \xi_{rr} = P(\xi, \eta) \quad (\text{A.15})$$

and

$$\eta_{zz} + \eta_{rr} = Q(\xi, \eta) \quad (\text{A.16})$$

are used, Eq. (A.11) reduces to

$$\frac{\partial^2}{\partial z^2} + \frac{\partial^2}{\partial r^2} = \frac{1}{J^2} \left(\alpha \frac{\partial^2}{\partial \xi^2} - 2\beta \frac{\partial^2}{\partial \xi \partial \eta} + \gamma \frac{\partial^2}{\partial \eta^2} \right) + P \frac{\partial}{\partial \xi} + Q \frac{\partial}{\partial \eta} \quad (\text{A.17})$$

Those relations derived above can be used to derive transformation equations listed below.

(1) From Eq. (A.14), the Laplace transformation equations in the computational plane become

$$\alpha z_{\xi\xi} - 2\beta z_{\xi\eta} + \gamma z_{\eta\eta} = 0 \quad (\text{A.18})$$

and

$$\alpha r_{\xi\xi} - 2\beta r_{\xi\eta} + \gamma r_{\eta\eta} = 0 \quad (\text{A.19})$$

(2) From Eq. (A.17), the Poisson transformation equations in the computational plane become

$$\alpha z_{\xi\xi} - 2\beta z_{\xi\eta} + \gamma z_{\eta\eta} = -J^2(Pz_{\xi} + Qz_{\eta}) \quad (\text{A.20})$$

and

$$\alpha r_{\xi\xi} - 2\beta r_{\xi\eta} + \gamma r_{\eta\eta} = -J^2(Pr_{\xi} + Qr_{\eta}) \quad (\text{A.21})$$

From these two equations, the source terms P and Q can be derived as

$$P = (z_{\eta}Dr - r_{\eta}Dz)/J^3 \quad (\text{A.22})$$

and

$$Q = (r_{\xi} Dz - z_{\xi} Dr) / J^3 \quad (\text{A.23})$$

where $Dr = \alpha r_{\xi\xi} - 2\beta r_{\xi\eta} + \gamma r_{\eta\eta}$ and $Dz = \alpha z_{\xi\xi} - 2\beta z_{\xi\eta} + \gamma z_{\eta\eta}$.

(3) With the use of Eqs. (A.7) and (A.17), the vorticity definition equation (2.2) in the computational plane takes the following form

$$\begin{aligned} \alpha \psi_{\xi\xi} - 2\beta \psi_{\xi\eta} + \gamma \psi_{\eta\eta} + (J^2 P + \frac{Jz_{\eta}}{r}) \psi_{\xi} + (J^2 Q - \frac{Jz_{\xi}}{r}) \psi_{\eta} \\ = -J^2 r \Omega \end{aligned} \quad (\text{A.24})$$

(4) With the use of Eqs. (A.6) and (A.7), the velocity equations (2.3) and (2.4) in the computational plane become

$$u = \frac{1}{Jr} (z_{\xi} \psi_{\eta} - z_{\eta} \psi_{\xi}) \quad (\text{A.25})$$

and

$$v = \frac{1}{Jr} (r_{\xi} \psi_{\eta} - r_{\eta} \psi_{\xi}) \quad (\text{A.26})$$

(5) With the use of Eqs. (A.6), (A.7), and (A.17), the vorticity transport equation (2.1) in the computational plane becomes

$$\begin{aligned} \alpha \Omega_{\xi\xi} - 2\beta \Omega_{\xi\eta} + \gamma \Omega_{\eta\eta} - \frac{J^2}{r^2} \Omega + (J^2 P - \frac{Jz_{\eta}}{r}) \Omega_{\xi} + (J^2 Q + \frac{Jz_{\xi}}{r}) \Omega_{\eta} \\ = \frac{JRe}{r} [(\psi_{\eta} \Omega_{\xi} - \psi_{\xi} \Omega_{\eta}) + \frac{\Omega}{r} (r_{\eta} \psi_{\xi} - r_{\xi} \psi_{\eta})] \end{aligned} \quad (\text{A.27})$$

(6) The energy equation (2.5) in the computational plane is also derived as

$$\begin{aligned} \alpha \theta_{\xi\xi} - 2\beta \theta_{\xi\eta} + \gamma \theta_{\eta\eta} + (J^2 P - \frac{Jz}{r} \eta) \theta_{\xi} + (J^2 Q + \frac{Jz}{r} \xi) \theta_{\eta} \\ = \frac{JPe}{r} (\psi_{\eta} \theta_{\xi} - \psi_{\xi} \theta_{\eta}) \end{aligned} \quad (\text{A.28})$$

Derivation of the governing equations in the computational plane is now complete. To derive boundary conditions, one must first derive the expressions for the normal and tangential vectors in the computational plane.

For a scalar function F in the physical plane, the gradient of F is

$$\nabla F = F_z \hat{e}_z + F_r \hat{e}_r \quad (\text{A.29})$$

This equation can be recast, with the use of (A.6) and (A.7), as

$$\nabla F = \frac{1}{J} [(r_{\eta} F_{\xi} - r_{\xi} F_{\eta}) \hat{e}_z + (-z_{\eta} F_{\xi} + z_{\xi} F_{\eta}) \hat{e}_r] \quad (\text{A.30})$$

On a line of constant η , $\eta_{\xi} = 0$ and $\eta_{\eta} = 1$; Eq. (A.30) reduces to

$$\nabla \eta = \frac{1}{J} (-r_{\xi} \hat{e}_z + z_{\xi} \hat{e}_r) \quad (\text{A.31})$$

Similarly, on a line of constant ξ , $\xi_\xi = 1$, $\xi_\eta = 0$, and

$$\nabla\xi = \frac{1}{J} (r_\eta \hat{e}_z - z_\eta \hat{e}_r) \quad (\text{A.32})$$

With reference to figure A.2, the unit normal vector to lines of constant η can be expressed as

$$\hat{n}(\eta) = \frac{\nabla\eta}{|\nabla\eta|} = \frac{-r_\xi \hat{e}_z + z_\xi \hat{e}_r}{\sqrt{\gamma}} \quad (\text{A.33})$$

The unit normal vector to lines of constant ξ is

$$\hat{n}(\xi) = \frac{\nabla\xi}{|\nabla\xi|} = \frac{r_\eta \hat{e}_z - z_\eta \hat{e}_r}{\sqrt{\alpha}} \quad (\text{A.34})$$

The unit tangent vectors can be derived with the use of cross products as follows:

$$\hat{t}(\eta) = \hat{n}(\eta) \times \hat{e}_\phi = \frac{z_\xi \hat{e}_z + r_\xi \hat{e}_r}{\sqrt{\gamma}} \quad (\text{A.35})$$

and

$$\hat{t}(\xi) = \hat{n}(\xi) \times \hat{e}_\phi = -\frac{z_\eta \hat{e}_z + r_\eta \hat{e}_r}{\sqrt{\alpha}} \quad (\text{A.36})$$

The directional derivatives of F along normal and tangential directions can be expressed as

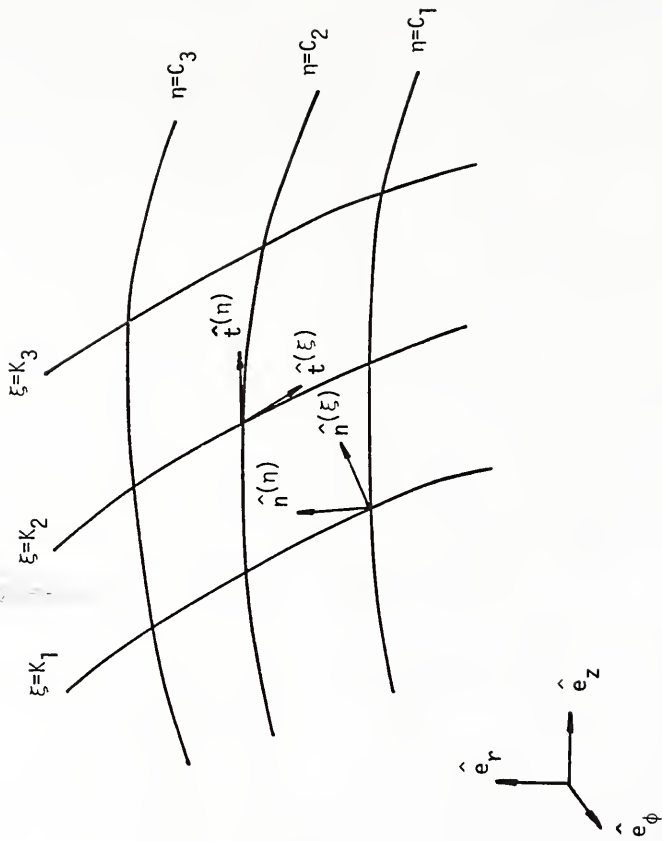


Figure A.2 Unit Tangent and Normal Vectors on Lines of Constant ξ and η

$$\frac{\partial F}{\partial \hat{n}(\eta)} = \hat{n}(\eta) \cdot \nabla F = \frac{1}{J} \frac{\gamma F_{\eta} - \beta F_{\xi}}{\sqrt{\gamma}} \quad (\text{A.37})$$

$$\frac{\partial F}{\partial \hat{t}(\eta)} = \hat{t}(\eta) \cdot \nabla F = \frac{F_{\xi}}{\sqrt{\gamma}} \quad (\text{A.38})$$

$$\frac{\partial F}{\partial \hat{n}(\xi)} = \hat{n}(\xi) \cdot \nabla F = \frac{1}{J} \frac{\alpha F_{\xi} - \beta F_{\eta}}{\sqrt{\alpha}} \quad (\text{A.39})$$

and

$$\frac{\partial F}{\partial \hat{t}(\xi)} = \hat{t}(\xi) \cdot \nabla F = - \frac{F_{\eta}}{\sqrt{\alpha}} \quad (\text{A.40})$$

The arc length dt along any contour Γ in the (z, r) plane is (see figure A.3)

$$dt^{(\Gamma)} = \sqrt{(dz)^2 + (dr)^2} \quad (\text{A.41})$$

In the transformed plane,

$$dt^{(\Gamma)} = \sqrt{\gamma(d\xi)^2 + \beta d\xi d\eta + \alpha(d\eta)^2} \quad (\text{A.42})$$

where (A.2) has been used for dz and dr .

If Γ is a line of constant η , Eq. (A.42) reduces to

$$dt^{(\eta)} = \sqrt{\gamma} d\xi \quad (\text{A.43})$$

Similarly, if Γ is a line of constant ξ , then

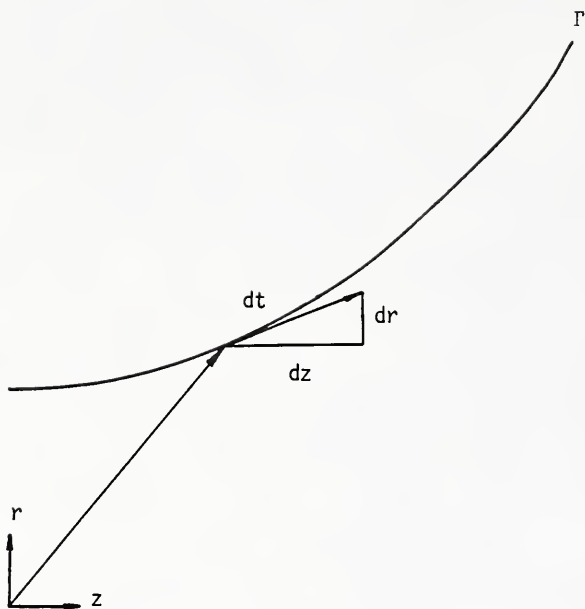


Figure A.3 Schematic Showing the Arc Length Along Contour r

$$dt^{(\xi)} = \sqrt{\alpha} \, d\eta \quad (\text{A.44})$$

Boundary conditions will now be derived in the transformed plane. Note that all conditions of the first kind can be used as is; no transformation is necessary of them. As for the other conditions, notice the fact that, in both inlet and exit domains B and C, grids are orthogonal in both original and transformed coordinates. So, metrics such as r_ξ , z_η , $r_{\xi\xi}$, and $z_{\eta\eta}$ all vanish. Furthermore, terms such as $r_{\xi\eta}$ and $r_{\eta\xi}$ also vanish because

$$r_{\xi\eta} = \frac{\partial}{\partial \xi} \left(\frac{\partial r}{\partial \eta} \right) = \frac{\partial}{\partial \eta} \left(\frac{\partial r}{\partial \xi} \right) = r_{\eta\xi} \quad (\text{A.45})$$

and $r_\xi = 0$.

With these in mind, consider Eq. (2.7a) first. It is clear that this condition is equivalent to

$$u_\xi = v_\xi = \psi_\xi = \Omega_\xi = 0 \quad (\text{A.46})$$

Next consider Eq. (2.7b). To express it in the transformed plane requires use of Eq. (A.8) in which the last three partial differentials all vanish because $n_z = 0$. The remaining two terms on the right-hand side of this equation may be transformed by use of Eqs. (A.5) and (A.6). It follows that

$$\theta_{\xi\xi} = \frac{z_{\xi\xi}}{z_{\xi}} \theta_{\xi} \quad (\text{A.47})$$

Along the axis of symmetry, that condition $u_r = 0$ is changed to

$$z_{\xi} u_{\eta} - z_{\eta} u_{\xi} = 0 \quad (\text{A.48})$$

using (A.7). Similarly, $\theta_r = 0$ becomes

$$z_{\xi} \theta_{\eta} - z_{\eta} \theta_{\xi} = 0 \quad (\text{A.49})$$

At the outer pipe wall, $\theta_{\eta} = 0$ is changed to

$$\gamma \theta_{\eta} - \beta \theta_{\xi} = 0 \quad (\text{A.50})$$

because of (A.37).

The vorticity boundary conditions at the inner and outer pipe walls can be derived using a lengthy procedure as follows.

At the wall, $u = v = 0$; Eqs. (4.3) and (4.4) become

$$z_{\xi} \psi_{\eta} - z_{\eta} \psi_{\xi} = 0 \quad (\text{A.51})$$

and

$$r_{\xi} \psi_{\eta} - r_{\eta} \psi_{\xi} = 0 \quad (\text{A.52})$$

These walls may be regarded as streamlines along which

$$\psi_{\xi} = 0 \quad (\text{A.53})$$

everywhere.

Using this relation in (A.51) yields

$$\psi_{\eta} = 0 \quad (\text{A.54})$$

which is also valid everywhere along the wall.

Differentiating Eq. (4.3) with respect to ξ gives

$$\begin{aligned} u_{\xi} &= \frac{\partial}{\partial \xi} \left[\frac{1}{Jr} (z_{\xi} \psi_{\eta} - z_{\eta} \psi_{\xi}) \right] \\ &= \frac{(Jr) \frac{\partial}{\partial \xi} (z_{\xi} \psi_{\eta} - z_{\eta} \psi_{\xi}) - (z_{\xi} \psi_{\eta} - z_{\eta} \psi_{\xi}) \frac{\partial}{\partial \xi} (Jr)}{(Jr)^2} \end{aligned} \quad (\text{A.55})$$

where the second term in the numerator vanishes because of (A.53) and (A.54). It follows that

$$u_{\xi} = \frac{1}{Jr} (z_{\xi\xi} \psi_{\eta} + z_{\xi} \psi_{\xi\eta} - z_{\xi\eta} \psi_{\xi} - z_{\eta} \psi_{\xi\xi}) \quad (\text{A.56})$$

Along the wall, $u_{\xi} = 0$. Also notice that (A.53) can be used to write

$$\psi_{\xi\xi} = 0 \quad (\text{A.57})$$

Then

$$\psi_{\xi\eta} = 0 \quad (\text{A.58})$$

from Eq. (A.56).

Equations (A.53), (A.54), (A.57), and (A.58) may now be used in (4.2) to write Ω at the wall as

$$\Omega_w = -\frac{\gamma}{J^2 r} \psi_{nn} \quad (\text{A.59})$$

APPENDIX B
DERIVATION AND USE OF EQUATION (3.6)

This appendix gives the details on how Eq. (3.6) is derived and used to locate grid lines in z direction.

It is necessary to locate the grid lines in figure (B.1) so that z_0 corresponds to index i_0 , z_1 to i_1 , z_i to i_i , z_{f-1} to i_{f-1} , and finally z_f to i_f . In particular, because of the z_i function to be chosen later, it is necessary that the following conditions be met

$$z_i = z_1 \quad \text{for } i_i = i_1 \quad (\text{B.1})$$

$$z_i = z_{f-1} \quad \text{for } i_i = i_{f-1} \quad (\text{B.2})$$

$$z_i = z_f \quad \text{for } i_i = i_f \quad (\text{B.3})$$

In order to meet the other conditions mentioned, but not formulated above, z_i is chosen to be a cubic polynomial of the form

$$z_i = z_0 + a_1 \psi_i + a_2 \psi_i^2 + a_3 \psi_i^3 \quad (\text{B.4})$$

where

$$\psi_i = \frac{i_i - i_0}{i_f - i_0}$$



Figure B.1 Indexing z Axis for Eq. (B.4)

There are three unknown coefficients (a_1 , a_2 , a_3) in Eq. (B.4) and there are three conditions ((B.1), (B.2), (B.3)) to solve them. These coefficients are found to be

$$a_1 = z_f - z_0 - a_2 - a_3 \quad (\text{B.5})$$

$$a_2 = [\Delta z_1 - h(z_f - z_0) - a_3(h^3 - h)]/(h^2 - h) \quad (\text{B.6})$$

$$a_3 = [\Delta z_f + \Delta z_1 - 2h(z_f - z_0)]/(h - 3h^2 + 2h^3) \quad (\text{B.7})$$

where

$$\Delta z_1 = z_1 - z_0$$

$$\Delta z_f = z_f - z_{f-1}$$

$$h = (i_f - i_0)^{-1}$$

In practice, values of i_0 , i_f , z_0 , z_f , Δz_1 and Δz_f must be preassigned. With suitable values of Δz_1 and Δz_f (to be tested), Eq. (B.4) yields a monotonous function of increasing grid sizes from z_0 to z_f .

APPENDIX C
DERIVATION OF FINITE DIFFERENCE EQUATIONS

Transformation equations (3.3) and (3.4) and governing equations (4.1) and (4.5) will be changed to finite-difference forms in this appendix. For the ease of formulation of these equations and later computation in the transformed plane, the grids in the computational plane are taken to be squares, i.e., $\Delta\xi = \Delta\eta = 1$. In the indexing scheme, i refers to ξ and j , η axis.

Defining $F = F(\xi, \eta)$ as a twice differentiable function of ξ and η , the finite difference representations for the first and second derivatives of F at an interior point (i, j) may be expressed, by means of a second-order central difference scheme, as follows:

$$(F_{\xi})_{i,j} = (F_{i+1,j} - F_{i-1,j})/2 \quad (C.1)$$

$$(F_{\eta})_{i,j} = (F_{i,j+1} - F_{i,j-1})/2 \quad (C.2)$$

$$(F_{\xi\xi})_{i,j} = F_{i+1,j} - 2F_{i,j} + F_{i-1,j} \quad (C.3)$$

$$(F_{\xi\eta})_{i,j} = (F_{i+1,j+1} - F_{i+1,j-1} + F_{i-1,j-1} - F_{i-1,j+1})/4 \quad (C.4)$$

and

$$(F_{\eta\eta})_{i,j} = F_{i,j+1} - 2F_{i,j} + F_{i,j-1} \quad (C.5)$$

The first-order backward and forward differences of F_{ξ} and F_{η} are given respectively as

$$(F_{\xi})_{i,j} = F_{i,j} - F_{i-1,j} \quad (C.6)$$

$$(F_{\eta})_{i,j} = F_{i,j} - F_{i,j-1} \quad (C.7)$$

and

$$(F_{\xi})_{i,j} = F_{i+1,j} - F_{i,j} \quad (C.8)$$

$$(F_{\eta})_{i,j} = F_{i,j+1} - F_{i,j} \quad (C.9)$$

To facilitate representation of partial differentials in computer programs, the changes of F in both ξ and η directions are written compactly as

$$\bar{F}_{\xi} = F_{i+1,j} - F_{i-1,j} \quad (C.10)$$

$$\bar{F}_{\eta} = F_{i,j+1} - F_{i,j-1} \quad (C.11)$$

and

$$\begin{aligned} \bar{F}_{\xi\eta} = & F_{i+1,j+1} - F_{i+1,j-1} + F_{i-1,j-1} \\ & - F_{i-1,j+1} \end{aligned} \quad (C.12)$$

Then, the transformation parameters α , β , γ , J , P , and Q become

$$\alpha = (\bar{z}_\eta^2 + \bar{r}_\eta^2)/4$$

$$\beta = (\bar{z}_\xi \bar{z}_\eta + \bar{r}_\xi \bar{r}_\eta)/4$$

$$\gamma = (\bar{z}_\xi^2 + \bar{r}_\xi^2)/4$$

$$J = (\bar{z}_\xi \bar{r}_\eta + \bar{z}_\eta \bar{r}_\xi)/4$$

$$P = (\bar{z}_\eta D r - \bar{r}_\eta D z)/(2J^3)$$

and

$$Q = (\bar{r}_\xi D z - \bar{z}_\xi D r)/(2J^3)$$

where

$$D r = \alpha(r_{\xi\xi})_{i,j} - 2\beta(r_{\xi\eta})_{i,j} + \gamma(r_{\eta\eta})_{i,j}$$

and

$$D z = \alpha(z_{\xi\xi})_{i,j} - 2\beta(z_{\xi\eta})_{i,j} + \gamma(z_{\eta\eta})_{i,j}$$

The transformation equations (3.3) and (3.4) take the following forms in the computational plane

$$\begin{aligned} \alpha z_{i-1,j} - 2(\alpha+\gamma)z_{i,j} + \alpha z_{i+1,j} = \\ -\gamma(z_{i,j+1} + z_{i,j-1}) + \frac{\beta}{2} \bar{z}_{\xi\eta} \end{aligned} \quad (C.13)$$

and

$$\begin{aligned} \alpha r_{i-1,j} - 2(\alpha+\gamma)r_{i,j} + \alpha r_{i+1,j} = \\ -\gamma(r_{i,j+1} + r_{i,j-1}) + \frac{\beta}{2} \bar{r}_{\xi\eta} \end{aligned} \quad (C.14)$$

These equations are to be used to map the grid points from the computational plane to the physical plane.

With the finite difference equations given above, the governing equations in Chapter IV can be changed to finite-difference forms as follows:

Vorticity transport equation:

$$\begin{aligned}
 & [2(\alpha+\gamma) + \frac{J^2}{r^2} + \operatorname{Re}(\frac{\bar{r}_n}{4r^2} \bar{\psi}_\xi - \frac{\bar{r}_\xi}{4r^2} \bar{\psi}_n)] \Omega_{i,j} \\
 &= [\alpha + \frac{1}{2}(J^2_P - \frac{J\bar{z}_n}{2r})] \Omega_{i+1,j} + [\alpha - \frac{1}{2}(J^2_P - \frac{J\bar{z}_n}{2r})] \Omega_{i-1,j} \\
 &+ [\gamma + \frac{1}{2}(J^2_Q + \frac{J\bar{z}_\xi}{2r})] \Omega_{i,j+1} + [\gamma - \frac{1}{2}(J^2_Q + \frac{J\bar{z}_\xi}{2r})] \Omega_{i,j-1} \\
 &- \operatorname{Re} \frac{J}{4r} \bar{\psi}_n \bar{\Omega}_\xi + \operatorname{Re} \frac{J}{4r} \bar{\psi}_\xi \bar{\Omega}_n - \frac{\beta}{2} \bar{\Omega}_{\xi n} \quad (C.15)
 \end{aligned}$$

Vorticity definition equation:

$$\begin{aligned}
 & 2(\alpha+\gamma) \psi_{i,j} \\
 &= [\alpha + \frac{1}{2}(J^2_P + \frac{J\bar{z}_n}{2r})] \psi_{i+1,j} + [\alpha - \frac{1}{2}(J^2_P + \frac{J\bar{z}_n}{2r})] \psi_{i-1,j} \\
 &+ [\gamma + \frac{1}{2}(J^2_Q - \frac{J\bar{z}_\xi}{2r})] \psi_{i,j+1} + [\gamma - \frac{1}{2}(J^2_Q - \frac{J\bar{z}_\xi}{2r})] \psi_{i,j-1} \\
 &+ J^2 r \Omega_{i,j} - \frac{\beta}{2} \bar{\psi}_{\xi n} \quad (C.16)
 \end{aligned}$$

Velocity equations:

$$u_{i,j} = \frac{\bar{z}_\xi}{4Jr} \bar{\psi}_n - \frac{\bar{z}_n}{4Jr} \bar{\psi}_\xi \quad (C.17)$$

$$v_{i,j} = \frac{\bar{r}_\xi}{4Jr} \bar{\psi}_\eta - \frac{\bar{r}_\eta}{4Jr} \bar{\psi}_\xi \quad (\text{C.18})$$

Energy equation:

$$\begin{aligned} & 2(\alpha+\gamma)\theta_{i,j} \\ &= \left[\alpha + \frac{1}{2}(J^2P - \frac{J\bar{z}_\eta}{2r}) \right] \theta_{i+1,j} + \left[\alpha - \frac{1}{2}(J^2P - \frac{J\bar{z}_\eta}{2r}) \right] \theta_{i-1,j} \\ &+ \left[\gamma + \frac{1}{2}(J^2Q + \frac{J\bar{z}_\xi}{2r}) \right] \theta_{i,j+1} + \left[\gamma - \frac{1}{2}(J^2Q + \frac{J\bar{z}_\xi}{2r}) \right] \theta_{i,j-1} \\ &- Pe \frac{J}{4r} \bar{\psi}_\eta \bar{\theta}_\xi + Pe \frac{J}{4r} \bar{\psi}_\xi \bar{\theta}_\eta - \frac{\beta}{2} \bar{\theta}_{\xi\eta} \end{aligned} \quad (\text{C.19})$$

It is convenient to introduce the following expressions for metric coefficients

$$C0 = -\beta/2$$

$$C1 = 2(\alpha+\gamma)$$

$$C2 = \alpha + (J^2P + \frac{J\bar{z}_\eta}{2r})/2$$

$$C3 = \alpha - (J^2P + \frac{J\bar{z}_\eta}{2r})/2$$

$$C4 = \gamma + (J^2Q - \frac{J\bar{z}_\xi}{2r})/2$$

$$C5 = \gamma - (J^2Q - \frac{J\bar{z}_\xi}{2r})/2$$

$$C6 = J^2r$$

$$C7 = 2(\alpha+\gamma) + J^2/r^2$$

$$C8 = \alpha + (J^2P - \frac{J\bar{z}_\eta}{2r})/2$$

$$C9 = \alpha - (J^2P - \frac{J\bar{z}_\eta}{2r})/2$$

$$C10 = \gamma + (J^2Q + \frac{J\bar{z}_\xi}{2r})/2$$

$$C11 = \gamma - (J^2Q + \frac{J\bar{z}_\xi}{2r})/2$$

$$C12 = \bar{z}_\xi / (4Jr)$$

$$C13 = \bar{z}_\eta / (4Jr)$$

$$C14 = \bar{r}_\xi / (4Jr)$$

$$C15 = \bar{r}_\eta / (4Jr)$$

$$C16 = J / (4r)$$

$$C17 = (J\bar{r}_\eta) / (4r^2)$$

and

$$C18 = (J\bar{r}_\xi) / (4r^2)$$

so that Eqs. (C.15) to (C.19) can be recast compactly as

$$\begin{aligned} & [C7 + \text{Re}(C17\bar{\psi}_\xi - C18\bar{\psi}_\eta)]_{\Omega_{i,j}} \\ & = C8\Omega_{i+1,j} + C9\Omega_{i-1,j} + C10\Omega_{i,j+1} + C11\Omega_{i,j-1} \\ & - \text{Re}C16(\bar{\psi}_\eta\bar{\Omega}_\xi - \bar{\psi}_\xi\bar{\Omega}_\eta) + C0\bar{\Omega}_{\xi\eta} \end{aligned} \quad (C.20)$$

$$\begin{aligned}
C1\psi_{i,j} &= C2\psi_{i+1,j} + C3\psi_{i-1,j} + C4\psi_{i,j+1} + C5\psi_{i,j-1} \\
&+ C6\Omega_{i,j} + C0\bar{\psi}_{\xi\eta} \quad \bullet \quad (C.21)
\end{aligned}$$

$$u_{i,j} = C12\bar{\psi}_{\eta} - C13\bar{\psi}_{\xi} \quad (C.22)$$

$$v_{i,j} = C14\bar{\psi}_{\eta} - C15\bar{\psi}_{\xi} \quad (C.23)$$

and

$$\begin{aligned}
C1\theta_{i,j} &= C8\theta_{i+1,j} + C9\theta_{i-1,j} + C10\theta_{i,j+1} + C11\theta_{i,j-1} \\
&- PeC16(\bar{\psi}_{\eta}\bar{\theta}_{\xi} + \bar{\psi}_{\xi}\bar{\theta}_{\eta}) + C0\bar{\theta}_{\xi\eta} \quad (C.24)
\end{aligned}$$

Rearranging the right-hand sides of Eqs. (C.20) and (C.24) yield

$$\begin{aligned}
&[C7 + \text{Re}(C17\bar{\psi}_{\xi} - C18\bar{\psi}_{\eta})]\Omega_{i,j} \\
&= (C8 - \text{Re}C16\bar{\psi}_{\eta})\Omega_{i+1,j} + (C9 + \text{Re}C16\bar{\psi}_{\eta})\Omega_{i-1,j} \\
&+ (C10 + \text{Re}C16\bar{\psi}_{\xi})\Omega_{i,j+1} + (C11 - \text{Re}C16\bar{\psi}_{\xi})\Omega_{i,j-1} \\
&+ C0\bar{\Omega}_{\xi\eta} \quad (C.25)
\end{aligned}$$

and

$$\begin{aligned}
C1\theta_{i,j} &= (C8 - PeC16\bar{\psi}_{\eta})\theta_{i+1,j} + (C9 + PeC16\bar{\psi}_{\eta})\theta_{i-1,j} \\
&+ (C10 + PeC16\bar{\psi}_{\xi})\theta_{i,j+1} + (C11 - PeC16\bar{\psi}_{\xi})\theta_{i,j-1} \\
&+ C0\bar{\theta}_{\xi\eta} \quad (C.26)
\end{aligned}$$

Equations (C.21) to (C.23) and (C.25) and (C.26) are the

central-difference versions of the original governing partial-differential-equations.

The numerical solution of Eqs. (C.25) and (C.26) may present a problem because it does not always converge. In order to rectify this problem, one way to do it is to make the diagonal dominant in the matrix expressions for these equations. Notice that the up-wind method cannot be directly used here because the convection terms in those transport equations have been simplified to the extent that their original formats have lost. Use is thus made of Takemitsu's method which is slightly modified as presented below.

There are four terms on the right-hand side of Eq. (C.25) that can be regrouped to relate convection as

$$\begin{aligned}
 CV = \text{Re} [& - C16\bar{\psi}_\eta (\Omega_{i+1,j} - \Omega_{i-1,j}) \\
 & + C16\bar{\psi}_\xi (\Omega_{i,j+1} - \Omega_{i,j-1})] \quad (C.27)
 \end{aligned}$$

Introducing

$$U = C16\bar{\psi}_\eta, \quad V = - C16\bar{\psi}_\xi \quad (C.28)$$

permits rewriting Eq. (C.27) more compactly as

$$CV = \text{Re} [- U(\Omega_{i+1,j} - \Omega_{i-1,j}) - V(\Omega_{i,j+1} - \Omega_{i,j-1})] \quad (C.29)$$

Notice that C16 is always positive, while $\bar{\psi}_\eta$ and $\bar{\psi}_\xi$ may change sign, depending on the local stream function. The terms in Eq. (C.29) have been written in central difference forms and they must be changed to either forward or backward difference to assure a convergent solution. Experience shows its choice hinges on the sign of U and V; a forward difference must be used if either of them is negative and vice versa. To meet these requirements, Eq. (C.29) is written as

$$CV = \text{Re}[- U(\Omega_{i+1,j} - \Omega_{i-1,j}) + |U| (\Omega_{i+1,j} - \Omega_{i,j} - \Omega_{i,j} + \Omega_{i-1,j}) - V(\Omega_{i,j+1} - \Omega_{i,j-1}) + |V| (\Omega_{i,j+1} - \Omega_{i,j} - \Omega_{i,j} + \Omega_{i,j-1})] \quad (\text{C.30})$$

which reduces to the following four situations

(i) U and V are both positive:

$$CV = 2\text{Re}[- U(\Omega_{i,j} - \Omega_{i-1,j}) - V(\Omega_{i,j} - \Omega_{i,j-1})] \quad (\text{C.31})$$

(ii) U is positive and V is negative:

$$CV = 2\text{Re}[- U(\Omega_{i,j} - \Omega_{i-1,j}) - V(\Omega_{i,j+1} - \Omega_{i,j})] \quad (\text{C.32})$$

(iii) U is negative and V is positive:

$$CV = 2\text{Re}[- U(\Omega_{i+1,j} - \Omega_{i,j}) - V(\Omega_{i,j} - \Omega_{i,j-1})] \quad (\text{C.33})$$

(iv) U and V are both negative:

$$CV = 2\text{Re}[-U(\Omega_{i+1,j} - \Omega_{i,j}) - V(\Omega_{i,j+1} - \Omega_{i,j})] \quad (\text{C.34})$$

The general form of CV, Eq. (C.30), is now substituted in Eq. (C.25) and with some regrouping of terms changes the latter to

$$\begin{aligned} & \{C7 + \text{Re}[C17\bar{\psi}_\xi - C18\bar{\psi}_\eta + 2(|U| + |V|)]\}_{\Omega_{i,j}} \\ & = [C8 - \text{Re}(U - |U|)]_{\Omega_{i+1,j}} + [C9 + \text{Re}(U + |U|)]_{\Omega_{i-1,j}} \\ & + [C10 - \text{Re}(V - |V|)]_{\Omega_{i,j+1}} + [C11 + \text{Re}(V + |V|)]_{\Omega_{i,j-1}} \\ & + C0\bar{\Omega}_{\xi\eta} \end{aligned} \quad (\text{C.35})$$

Following the similar approach, a general form of the energy equation is derived as

$$\begin{aligned} & [C1 + 2\text{Pe}(|U| + |V|)]_{\theta_{i,j}} \\ & = [C8 - \text{Pe}(U - |U|)]_{\theta_{i+1,j}} + [C9 + \text{Pe}(U + |U|)]_{\theta_{i-1,j}} \\ & + [C10 - \text{Pe}(V - |V|)]_{\theta_{i,j+1}} + [C11 + \text{Pe}(V + |V|)]_{\theta_{i,j-1}} \\ & + C0\bar{\theta}_{\xi\eta} \end{aligned} \quad (\text{C.36})$$

These equations will lead to a convergent solution.

In closing this appendix, a short note is included to show that the scheme developed above is rooted in the upwind scheme mentioned earlier. According to this scheme,

it is necessary to consider the flow retains its past identity when it is migrated to a new location. The backward and forward representations of Ω discussed above indeed come from this origin. In fact, it can be shown that the sign of U and V are related to that of u and v , which can be verified by using those equations in domain B .

APPENDIX D
DERIVATION OF PRESSURE GRADIENT EQUATIONS

The expressions for pressure gradients in z and r directions at the wall will be derived in this appendix. In the derivation, the Navier-Stokes equations will be used together with the continuity equation to derive the pressure gradient expressions. Finally, the vorticity definition is introduced to reduce the differential order in the final expressions.

For axisymmetrical flow of an incompressible medium in a cylindrical pipe or annulus, the nondimensional continuity equation and momentum equations are given as follows:

$$\frac{\partial u}{\partial z} + \frac{\partial v}{\partial r} + \frac{v}{r} = 0 \quad (D.1)$$

$$u \frac{\partial u}{\partial z} + v \frac{\partial u}{\partial r} = - \frac{\partial p}{\partial z} + \frac{1}{\text{Re}} \left(\frac{\partial^2 u}{\partial z^2} + \frac{\partial^2 u}{\partial r^2} + \frac{1}{r} \frac{\partial u}{\partial r} \right) \quad (D.2)$$

and

$$u \frac{\partial v}{\partial z} + v \frac{\partial v}{\partial r} = - \frac{\partial p}{\partial r} + \frac{1}{\text{Re}} \left(\frac{\partial^2 v}{\partial z^2} + \frac{\partial^2 v}{\partial r^2} + \frac{1}{r} \frac{\partial v}{\partial r} - \frac{v}{r^2} \right) \quad (D.3)$$

where

$$p = p^* / (\rho u_m^{*2})$$

Equation (D.2) is used to write the pressure gradient in z direction at the wall as

$$\frac{\partial p}{\partial z} = \frac{1}{\text{Re}} \left(\frac{\partial^2 u}{\partial z^2} + \frac{\partial^2 u}{\partial r^2} + \frac{1}{r} \frac{\partial u}{\partial r} \right) \quad (\text{D.4})$$

The continuity equation is differentiated with respect to z

$$\frac{\partial^2 u}{\partial z^2} = - \frac{\partial^2 v}{\partial z \partial r} - \frac{1}{r} \frac{\partial v}{\partial z} \quad (\text{D.5})$$

and substituted into (D.4) to give

$$\frac{\partial p}{\partial z} = \frac{1}{\text{Re}} \left(\frac{\partial^2 u}{\partial r^2} - \frac{\partial^2 v}{\partial z \partial r} + \frac{1}{r} \frac{\partial u}{\partial r} - \frac{1}{r} \frac{\partial v}{\partial z} \right) \quad (\text{D.6})$$

Recall that the vorticity is defined as

$$\Omega = \frac{\partial v}{\partial z} - \frac{\partial u}{\partial r} \quad (\text{D.7})$$

Differentiating this equation with respect to r gives

$$\frac{\partial \Omega}{\partial r} = \frac{\partial^2 v}{\partial z \partial r} - \frac{\partial^2 u}{\partial r^2} \quad (\text{D.8})$$

Introducing these two equations into (D.6) gives the final expression for the pressure gradient in z direction at the wall

$$\frac{\partial p}{\partial z} = - \frac{1}{\text{Re}} \left(\frac{1}{r} \frac{\partial r \Omega}{\partial r} \right) \quad (\text{D.9})$$

The pressure gradient in r direction at the wall may be derived by following a similar procedure. Equation (D.3) will be used instead, and this equation is simplified by using the condition that $u = v = 0$ at the wall. It follows that

$$\frac{\partial p}{\partial r} = \frac{1}{\text{Re}} \left(\frac{\partial^2 v}{\partial z^2} + \frac{\partial^2 v}{\partial r^2} + \frac{1}{r} \frac{\partial v}{\partial r} \right) \quad (\text{D.10})$$

Equation (D.1) is differentiated with respect to r

$$- \frac{\partial^2 u}{\partial r \partial z} = \frac{\partial^2 v}{\partial r^2} + \frac{1}{r} \frac{\partial v}{\partial r} - \frac{v}{r^2} \quad (\text{D.11})$$

and Eq. (D.7) is differentiated with respect to z to give

$$\frac{\partial \Omega}{\partial z} = \frac{\partial^2 v}{\partial z^2} - \frac{\partial^2 u}{\partial r \partial z} \quad (\text{D.12})$$

and finally introducing these two equations into (D.10) gives the pressure gradient in r direction at the wall as

$$\frac{\partial p}{\partial r} = \frac{1}{\text{Re}} \frac{\partial \Omega}{\partial z} \quad (\text{D.13})$$

REFERENCES

1. Hurd, N. L., "Mean Temperature Difference in the Field or Bayonet Tube," *Industrial and Engineering Chemistry*, Volume 38, Number 12, 1946, pp. 1266-1271.
2. Beekly, D. C., and Mather, G. R., "Analysis and Experimental Test of a High-Performance, Evacuated Tubular Collector," NASA, CR-150874, 1978.
3. Moan, K. L., An Analysis of the Low Loss Evacuated Tubular Collector Using Air as the Heat Transfer Fluid, Owens-Illinois, Inc., Toledo, Ohio. Unpublished report.
4. Shah, R. K., and London, A. L., *Laminar Flow Forced Convection in Ducts*, *Advances in Heat Transfer*, Supplement 1, Academic Press, Inc., New York, 1978.
5. Ehrlich, L. W., "The Numerical Solution of a Navier-Stokes Problem in a Stenosed Tube: A Danger in Boundary Approximations of Implicit Marching Schemes," *Computer and Fluid*, Volume 7, 1979, pp. 247-256.
6. Gosman, A. D., Pun, W. M., Runchal, A. K., Spalding, D. B., and Wolfshtein, M., *Heat and Mass Transfer in Recirculating Flows*, Academic Press, Inc., London, 1969.
7. Singh, S. N., "Heat Transfer by Laminar Flow in a Cylindrical Tube," *Applied Scientific Research*, Section A, Volume 7, 1958, pp. 325-340.
8. Thompson, J. F., Thames, F. C., and Mastin, C. W., "Boundary-Fitted Curvilinear Coordinate Systems for Solution of Partial Differential Equation on Field Containing Any Number of Arbitrary Two-Dimensional Bodies," NASA, CR-2729, 1977.
9. Nietubicz, C. J., Heavey, K. R., and Steger, J. L., "Grid Generation Techniques for Projectile Configurations," *Proceedings of 1982 Army Numerical Analysis and Computer Conference*, Vicksburg, Mississippi. ARO Rept. 82-3, 1983.

10. Sorenson, R. L., and Steger, J. L., "Simplified Clustering of Nonorthogonal Grids Generated by Elliptic Partial Differential Equations," NASA, TM-73252, 1977.
11. Takemitsu, N., "On a Finite-Difference Approximation for the Steady-State Navier-Stokes Equations," Journal of Computational Physics, Volume 36, 1980, pp. 236-248.
12. Roache, P. J., Computational Fluid Dynamics, Revised Printing, Hermosa Publishers, Albuquerque, New Mexico, 1976.
13. Parmentier, E. M., and Torrance, K. E., "Kinematically Consistent Velocity Fields for Hydrodynamic Calculations in Curvilinear Coordinates," Journal of Computational Physics, Volume 19, 1975, pp. 404-417.
14. Rigal, A., "Acceleration of the Convergence in Viscous Flow Computations," Journal of Computational Physics, Volume 43, 1981, pp. 177-179.
15. Roache, P. J., "Semidirect Calculation of Steady Two- and Three-Dimensional Flows," in Numerical Methods in Laminar and Turbulent of the First International Conference, John Wiley & Sons, Inc., New York, 1978, pp. 17-27.
16. Miyakoda, K., "Contribution to the Numerical Weather Prediction--Computation with Finite Difference," Japanese Journal of Geophysics, Volume 3, 1962, pp. 75-190.
17. Bird, R. B., Stewart, W. E., and Lightfoot, E. N., Transport Phenomena, John Wiley & Sons, Inc., New York, 1960.
18. Kays, W. M., and Grawford, M. E., Convective Heat and Mass Transfer, Second Edition, McGraw-Hill, New York, 1980.
19. White, F. M., Viscous Fluid Flow, McGraw-Hill, New York, 1974.
20. Morihara, H., and Cheng, R. T.-S., "Numerical Solution of the Viscous Flow in the Entrance Region of Parallel Plates," Journal of Computational Physics, Volume 11, 1973, pp. 550-572.

21. Vrentas, J. S., Duda, J. L., and Bargeron, K. G., "Effect of Axial Diffusion of Vorticity on Flow Development in Circular Conducts: Part I. Numerical Solutions," A. I. Ch. E. Journal, Volume 12, Number 5, 1966, pp. 837-844.
22. Hornbeck, R.W., "Laminar Flow in the Entrance Region of a Pipe," Applied Scientific Research, Section A, Volume 13, 1964, pp. 224-232.
23. Hornbeck, R. W., "An All-Numerical Method for Heat Transfer in the Inlet of a Tube," American Society of Mechanical Engineering, Paper 65-WA/HT-36, 1965.
24. Lundberg, R. E., Reynold, W. C., and Kays, W. M., "Heat Transfer with Laminar Flow in Concentric Annuli with Constant and Variable Wall Temperature and Heat Flux," NASA, TN D-1972, 1963.
25. Carnahan, B., Luther, H. A., and Wilkes, J. O., Applied Numerical Method, John Wiley & Sons, Inc., New York, 1969.

BIOGRAPHICAL SKETCH

Song-Lin Yang, was born on November 6, 1952, in Hsinchuang, Taipei, Taiwan, Republic of China. He received his early childhood education in his hometown; and his high school education in Taipei. After graduation from high school, he entered Chung Yuan University, Chungli, Taiwan, where he received his Bachelor of Science degree in mechanical engineering (1976) and Master of Science degree in applied physics (1980). On March 7, 1981, he married Li-Pin Hsiao and now they have a lovely son named Albert Chung-Pu Yang.

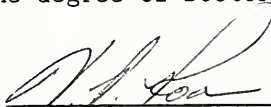
He is a student member of the American Society of Mechanical Engineers (ASME) and the American Society of Heating, Refrigeration and Air Conditioning Engineering (ASHRAE). He is also a member of Tau Beta Pi, the National Engineering Honor Society.

I certify that I have read this study and in my opinion it conforms to acceptable standards of scholarly presentation and is fully adequate, in scope and quality, as a dissertation for the degree of Doctor of Philosophy.



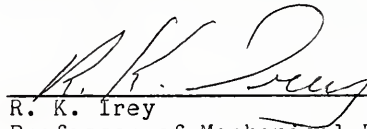
C. K. Hsieh, Chairman
Professor of Mechanical Engineering

I certify that I have read this study and in my opinion it conforms to acceptable standards of scholarly presentation and is fully adequate, in scope and quality, as a dissertation for the degree of Doctor of Philosophy.



V. P. Roan
Professor of Mechanical Engineering

I certify that I have read this study and in my opinion it conforms to acceptable standards of scholarly presentation and is fully adequate, in scope and quality, as a dissertation for the degree of Doctor of Philosophy.



R. K. Frey
Professor of Mechanical Engineering

I certify that I have read this study and in my opinion it conforms to acceptable standards of scholarly presentation and is fully adequate, in scope and quality, as a dissertation for the degree of Doctor of Philosophy.



C. C. Hsu
Professor of Engineering Science

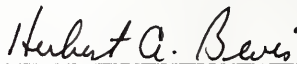
I certify that I have read this study and in my opinion it conforms to acceptable standards of scholarly presentation and is fully adequate, in scope and quality, as a dissertation for the degree of Doctor of Philosophy.



H. A. Ingley, III
Associate Professor of Mechanical
Engineering

This dissertation was submitted to the Graduate Faculty of the College of Engineering and to the Graduate School, and was accepted as partial fulfillment of the requirements for the degree of Doctor of Philosophy.

May, 1985



Dean, College of Engineering

Dean for Graduate Studies and
Research